POLITECNICO DI TORINO

Master's Degree in Aerospace Engineering - Space Engineering

Master's Degree Thesis

Multi-fidelity evaluation of aerodynamic coefficients for re-entry objects of arbitrary shapes

Politecnico di Torino

Supervisor
Prof. Paolo Maggiore

Candidate
Cristian Granata
s281523

Academic Year 2021-2022

Acknowledgments

Innanzitutto voglio ringraziare il mio Dio che mi ha sostenuto durante tutto questo percorso e in tutti i momenti della mia vita.

Un grande ringraziamento va al *Prof. Paolo Maggiore* per la sua grande disponibilità e per il suo supporto durante lo sviluppo di questa tesi.

I also want to thank the people that helped and supported me during my stay at VKI. First of all *Alessandro*, your support has been key for me and you are an inspiration for who I want to become, nothing of this experience would have been possible without you. A special thanks is also addressed to *Federico* and *Zuheyr*, your patience and your assistance helped me a lot. I also want to thank *Simone* and *Marco* who have been my everyday support even during the toughest moments of my stay in Belgium.

Tornando a Torino il mio primo pensiero è per te *Greta*, che sei stata la mia spalla in questi 5 anni a Torino nei momenti bui e nei momenti migliori. Non dimenticherò mai le depressioni post esami e le torte mangiate per festeggiare. Grazie di tutto.

Voglio anche ringraziare gli amici che sin dal primo anno sono stati al mio fianco e con i quali ho condiviso di tutto: *Alice*, *Stefano*, *Caterina* ed *Elia*. Tutte le esperienze e i ricordi che abbiamo passato le custodirò sempre gelosamente.

Voglio ancora ringraziare i miei amici della Xbox: *Ciccio*, *Ndonij*, e *Piova* siete stati indispensabili, le giornate a fare talking e le serate su Pro Club in vostra compagnia sono state il meglio che potessi chiedere per risollevarmi dalle giornate pesanti e staccare dallo studio. *Nello* e *Gennaro*, le serate trascorse su F1 e i momenti passati a sopportarmi nell'ultimo anno sono stati di grande aiuto. Grazie a tutti voi.

Un sentito ringraziamento va anche ad *Alberto*, non c'è giorno che non discutiamo e facciamo questione su qualsiasi cosa, ma la tua vicinanza e i tuoi consigli sono stati fondamentali. Grazie.

Un ringraziamento è necessario anche per tutti i colleghi, i compagni di progetto, la famiglia e le persone che negli ultimi anni hanno fatto parte della mia vita, avete tutti contribuito a farmi diventare ciò che sono e ve ne sono grato.

Uno speciale ringraziamento va a mia nonna *Nennella*, nonostante tu non sia più qui, sei stata fondamentale per la mia crescita e non sarei arrivato fin qui senza di te.

Per concludere, il mio più grande ringraziamento è per i miei genitori *Massimiliano* e *Michela* e per mia sorella *Roberta*, che nonostante la pandemia e le difficoltà mi hanno sempre sostenuto e dato tutto ciò di cui ho avuto bisogno e specialmente il vostro amore non è mai mancato. Il raggiungimento di questo traguardo è principalmente merito vostro, non trovo parole per spiegare ciò che significate per me. Vi voglio un bene immenso!

Summary

In recent years, the problem of space debris has become relevant and is now being studied to reduce the impact that has on the population. For this purpose, at the von Karman Institute for Fluid Dynamics, the project DSMCFED aims to develop a toolset to analyze the re-entry phase of spacecraft during their disposal.

The main objective is to simulate the spacecraft fragmentation during the descent into the atmosphere by coupling high-fidelity tools to analyze the aerothermodynamics, the trajectory, and the thermo-structural response. In this context, to compute the trajectory of the objects it is necessary to evaluate their aerodynamic coefficients at different altitudes, so a code to study the flow interaction with the body is needed.

Direct Simulation Monte Carlo has been identified as the method to solve the problem in the rarefied/transitional regime, however when the altitude decreases and the regime approaches the continuum, the computational cost associated with the simulations drastically increases; different approaches are sought to reduce the weight of the simulations to evaluate the aerodynamic coefficients of the objects at different configurations to perform the trajectory propagation.

This thesis aims to find alternative methods to complement DSMC analysis and reduce the time needed for the simulations while ensuring a good degree of accuracy.

In the first part, the reader is introduced to the addressed problem and to the aerodynamic theories useful to understand the discussion. Subsequently, the numerical solvers and the relative methods applied in the simulations are shown. Finally, the different test cases are defined and the simulation results are exhibited. Based on these considerations, a tentative approach has been drafted to complement the DSMC simulations using lower-fidelity software to reduce the computational cost related to the evaluation of the aerodynamic coefficients at different attitudes during the re-entry.

Contents

Nomenclature

Acronyms

ANTARES	Application of Newtonian Theory for ARbitrary Entry Shapes
AOA	Angle of Attack
BTE	Boltzmann Transport Equation
CFD	Computational Fluid Dynamics
DoF	Degree of Freedom
DSMC	Direct Simulation Monte Carlo
DSMCFED	Development of a Simulation Methodology for Coupled Fragmentation Estimation during Demise
MFP	Mean Free Path
MPI	Message Passing Interface
NRMSE	Normalized Root Mean Square Error
NS	Navier-Stokes
RMSE	Root Mean Square Error
SPARTA	Stochastic PArallel Rarefied-gas Time-accurate Analyzer
STL	StereoLithography
VKI	von Karman Institute
VSS	Variable Soft-Sphere

Symbols

γ	Heat Capacity Ratio
K_b	Boltzmann Constant
n	Number Density of Particles
p	Pressure
R	Specific Gas Constant
T	Temperature

Chapter 1

Introduction

The re-entry procedure is the last part of a satellite's life, it is important to understand how the objects behave during their descent into the atmosphere, to predict their trajectory and fragmentation for scientific and safety reasons. Space agencies are addressing the space debris problem, enforcing spacecraft manufacturers to ensure that the vehicles are disposed safely at their end of life. This process can be accomplished by moving the spacecraft into cemetery orbits or by using deorbiting devices to induce an atmospheric re-entry. The latter strategy needs a profound understanding of the dynamics of the satellite re-entry process among which: the fragmentation process, the trajectory propagation, and the demise steps for all the objects belonging to the spacecraft. The objects during the re-entry meet different flow conditions based on their dimensions and altitude, so different kinds of analysis can be carried out to understand their behavior. Among these, Computational Fluid Dynamics (CFD) and Direct Simulation Monte Carlo (DSMC) are the most widely used depending on the regime of interest; however, their computational cost is usually high, so different techniques can be experimented to improve the feasibility of the simulations. The first possibility is to perform 2D analysis to simplify the domain of the runs, although the outcome of the simulations will be affected by a lower degree of accuracy than a complete 3D simulation; the other option is to take several simplifications and couple multiple high-fidelity tools to take into account all the physical elements of the re-entry (i.e. aerothermodynamics, flow-surface interactions, fragmentation process) and perform the simulations in an acceptable time.

In this context, the activity DSMCFED (Development of a Simulation Methodology for Coupled Fragmentation Estimation during Demise) is conducted by VKI to complement engineering tools during the creation process of new spacecraft and secure adherence with Design for Demise guidelines. In particular, the project will provide a toolset able to simulate the spacecraft aerothermodynamics and the thermo-structural behavior in the rarefied and transitional regimes.

The final toolset will be made of three solvers that interact among them to

perform the numerical simulations:

- Trajectory propagator: solves the equation of motion in 6-DoF starting from a selected attitude.

- Flow code: computes the aerodynamic coefficients and the aerothermal loads of the objects during the descent, using a DSMC code.

- Thermo-structural code: estimates the reaction of the spacecraft to the evaluated aerothermal loads and defines the chain of failures that generate the fragments during the re-entry, using a FEM thermo-mechanical tool.

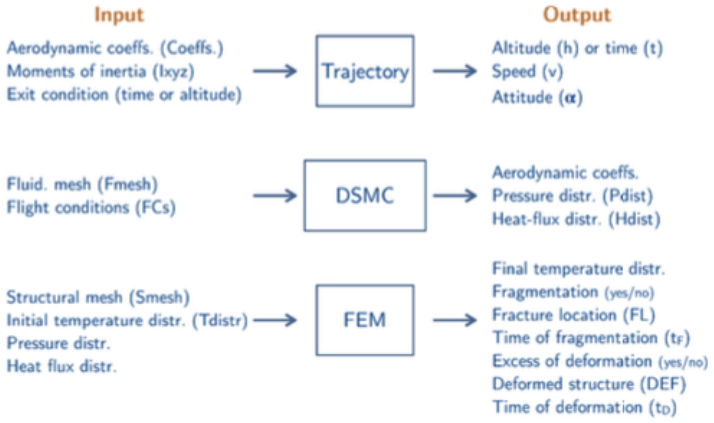

Figure 1.1: DSMCFED solvers interaction [43].

1.1 State of the Art

In this section, the studies already performed on the comparison between DSMC and other techniques for the estimation of the aerodynamic coefficients will be presented as a starting point for the work. Different studies have been conducted [9, 29, 32] on which kind of approach to use based on the degree of rarefaction of the flow encountered by a re-entry object as originally defined by Chambre [15]. A summary of the methods applicability field is shown in figure 1.2.

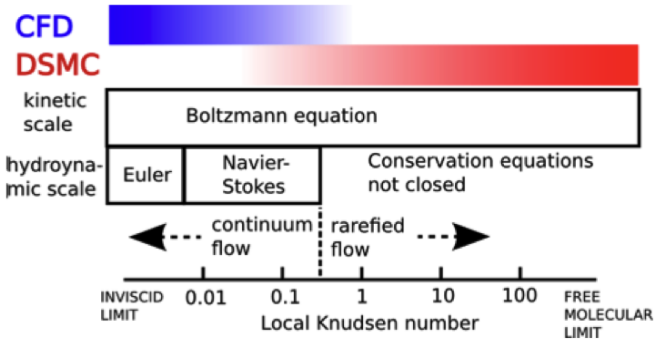

Figure 1.2: CFD-DSMC applicability with respect to local Knudsen number [33].

As a matter of fact, the Navier-Stokes equations are valid when the Knudsen number (defined as the ratio between the molecules mean free path over a reference length of the body) is under approximately 0.1, in this case, CFD analysis provide the most efficient/accurate results; however, NS equations lose their validity when the rarefaction effects in the flow are the dominant ones and the Knudsen number rises above 0.1. In this scenario, the approach based on the Boltzmann equation resolution as done by DSMC using a particle method is the preferred one, since a gas kinetic scale characterization has to be done. The latter approach could also be used in the continuum regime to replace CFD, however, the computational cost rises when a highly collisional region is encountered because a high number of particles and collisions have to be simulated. Based on these considerations, it is clear that in recent research the objective is to couple DSMC and CFD methods [45–47], using the local Knudsen number as a parameter, to optimize the hypersonic re-entry analysis for satellites.

On this matter, another important topic of research is the optimization of the computational cost for the DSMC simulations, while maintaining a low degree of error in the results. Different techniques have been tested, starting from the use of vector processing [38] to the optimization of the parallelization for the DSMC method [36].

A different approach is based on using strong simplifications in the analysis to reduce the number of simulated variables while trying to limit the errors obtained in the approximation. Some examples are shown in [34] and [25], where the limits of the free molecular theory with respect to DSMC are evidenced in failing to catch the boundary layer and the multi-species gas effects. Interesting practical results have been shown in [26], where the author compares the drag force results obtained using DSMC and the free molecular theory at different altitudes and in different flow regimes on a 3U CubeSat platform, showing that the comparison is extremely efficient when the flow is in free molecular conditions, moreover the analogy is still good considering a transitional flow at 90 km altitude, where the results show a maximum standard deviation lower than 20%.

1.2 Thesis Objectives

Starting from what has been pointed out before on the high computational cost of the analysis concerning the DSMC module, it is necessary to find a way to optimize the DSMCFED toolset simulation time while maintaining a good degree of accuracy in the results. The activity of this thesis is based on the DSMC module output, in particular, it refers to the estimation of the aerodynamic coefficients using lower fidelity tools to complement DSMC results. Necessarily, some simplifications will be applied and the accuracy of the coefficients with respect to DSMC will reduce, but the computational cost of the analyses will decrease, allowing the toolset to work in a much faster timeframe. To do so, a database for the aerodynamic coefficients of different shapes will be created in different flow regimes and different numerical tools will be compared. To conclude, a way to reduce the errors in the estimation between DSMC and the lower fidelity tools complemented results, will be sought.

1.3 Outline of the Thesis

This thesis is organized into 6 chapters, including the starting introduction extended with state-of-the-art research on the topic.

Chapter 2 provides an overview of the aerodynamic theories at the basis of this work; the gas kinetic theory and the Newtonian theory are recalled, then the general aerodynamic concepts used to extrapolate the results are shown.

In chapter 3 the codes used to perform the simulations are introduced with references to the methods employed by each of them.

In chapter 4, a specific description of the tested scenarios is shown for all the analyzed geometries and flow conditions, along with the simulation input for each of the used software.

In chapter 5, the simulations results are presented starting from a comparison among the different codes, and moving to the presentation of the proposed algorithm to minimize the errors between DSMC and the lower fidelity tools complemented results.

In chapter 6, conclusions are drawn, as well as some future work recommendations to proceed with this thesis activity.

Chapter 2

Physical Models and Theory

In this chapter, general concepts of the considered aerodynamic theories are shown. For starters a brief introduction is made to explain the physical quantities taken into analysis during the re-entry, then information about the gas kinetic theory is given. To conclude the Newtonian inviscid theory for hypersonic flows is introduced. All the given notions, provide the basis to understand the codes explained in chapter 3.

During the re-entry phase, satellites are subject to different atmospheric conditions, and the gas dynamics that make up the atmosphere can be modeled using two different approaches:

- **a microscopic approach**, where the system is described giving a characterization of the state of every molecule composing the gas, considering their internal state, position, and velocity.

- **a macroscopic approach**, where the gas is considered as a continuous medium characterized by basilar properties such as temperature, pressure, velocity, and density.

The accepted mathematical model for the macroscopic approach is given by the NS equations that describe the motion of a viscous flow using coupled differential equations, on the other side using the microscopic approach, the gas is characterized using the kinetic theory, in particular resolving the Boltzmann equation.

Considering that in gases the motion of particles is chaotic, they have full freedom of movement and their only mean of interaction among them is through collisions. Over the course of the descent of an object into the atmosphere, the environment density increases causing a rise in the number of particles encountered by the object and a subsequent reduction of the mean free path of particles in the gas, defined as the average distance traveled by a particle before hitting another particle, causing a change in the energy or direction of the movement. This parameter

can be defined using the ideal gas approximation as:

$$MFP = \lambda = \frac{K_b T}{\sqrt{2}\pi d^2 p} \tag{2.1}$$

where d stands for the diameter of the particles composing the flow and p is the flow pressure. Using the macroscopic approach, known also as continuum mechanics, the MFP is considered as 0, allowing the use of the NS equations to solve the problem. However, this approach can be used only at near-earth altitudes, since the mean free path simplification is valid.

To describe the flow around a descending body and select the approach to analyze the problem, the Knudsen number needs to be calculated. This parameter is an adimensional quantity defined as:

$$Kn = \frac{MFP}{L} \tag{2.2}$$

where L stands for the characteristic length of the body.
The Knudsen number determines the flow regime that develops around the body, to see if the continuum approach can be used. Different regimes can be identified when considering the Knudsen number:

- **Free molecular flow regime**: it represents the more rarefied regime, where the MFP is higher than the body characteristic length, so for convention [17], $Kn > 10$. In this scenario, the incident flow is considered undisturbed by the presence of the body, and no shock waves are assumed to be generated near the body because the boundary layer is extremely diffused.

- **Transitional flow regime**: this regime is considered when $0.1 < Kn < 10$. In this case, the fluid flow behavior is dependent on the size of the object and the effects of rarefaction start to disappear, causing the creation of a less diffused shock wave in front of the body invested by the flow.

- **Slip flow regime**: in this case $0.001 < Kn < 0.1$. The flow is starting to become less rarefied and the effects of compressibility, viscosity, and rarefaction are interrelated. In this regime, it is expected to see a shock wave in front of the body; the shock thickness decreases as it becomes less diffuse when the Knudsen number lowers, as the thickness is of the same order of magnitude as the MFP [39].

- **Continuum flow regime**: in this regime $Kn < 0.001$. The MFP value is close to 0 and the flow is distributed uniformly over the body.

Considering the described flow regimes, the approaches described above to treat the gas dynamics can be selected based on the Knudsen number of the flow. In

particular, when the flow is in the continuum or slip flow conditions, NS equations are valid and the problem can be solved using the continuum mechanics (CFD). When the effects of rarefaction increase and $Kn > 0.1$ the Boltzmann equation can be used to solve the problem taking advantage of the kinetic gas theory (DSMC).

A more clear classification of the usable approaches based on the Knudsen number definition is shown in figure 2.1.

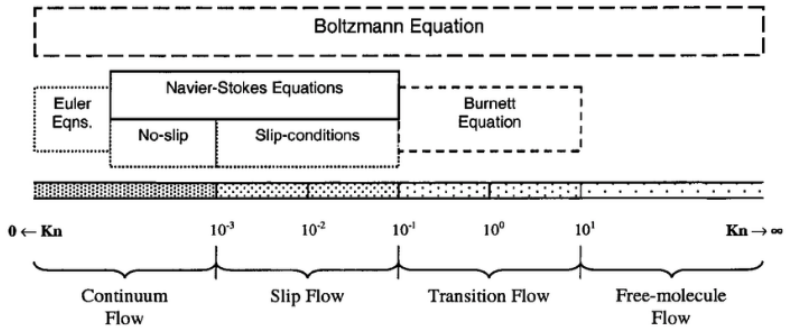

Figure 2.1: Approaches classification with respect to Knudsen number [44].

To complete the discussion, it is also necessary to introduce the Mach number as the ratio of the flow speed over the speed of sound in that flow:

$$M = \frac{v}{\sqrt{\gamma RT}} \tag{2.3}$$

During the re-entry phase, the Mach number value is in the hypersonic regime and can change significantly, which may strongly influence the trajectory and the field around the body.

2.1 Gas Kinetic Theory

In this section, some specific notions about the gas kinetic theory are presented.

Kinetic theory studies the microscopic behavior of particles belonging to a gas, analyzing their interaction to extract the macroscopic properties related to the gas, such as pressure and volume. 6 main assumptions are at the basis of the theory [27]:

1) The random motion of the molecules that make up the gas is possible in all directions.

2) The molecules that compose the gas are considered rigid, elastic spheres and the molecules are identical for the same gas.

3) The collision time between two particles is negligible.

4) The collisions among particles are completely elastic, so the forces of attraction and repulsion are null.

5) The volume occupied by the particles is neglectable with respect to the container volume.

6) The dimension of the molecules is smaller than the distance between them, which is defined as the mean molecular distance:

$$\delta = \frac{1}{n^{1/3}} \tag{2.4}$$

where n stands for the number density of particles $[1/m^3]$.

Following these assumptions, it is possible to consider that each molecule exercises a force on the other particles, this attractive force decreases when the particles are at a high distance, while it rises when the particles approach each other; it becomes a repulsive force when the distance between particles approaches 0. Figure 2.2 shows the behavior of the intermolecular force depending on the distance between particles.

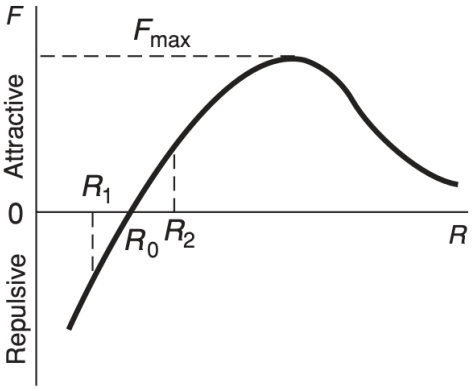

Figure 2.2: Intermolecular forces with respect to distance among molecules [28].

When the density of the particles is low, the mean molecular distance δ is much bigger than the molecular diameter, so the number of interactions among molecules is so low that only binary collisions between two particles are considered as a valid assumption. This consideration determines a dilute gas.

In this regard, it is possible to describe the gas at a microscopic level using three different variables for each molecule: its internal state, its position $\mathbf{r} = (x, y, z)$ and its velocity $\mathbf{v} = (v_x, v_y, v_z)$. The best approach to solve a problem considering that the number of molecules in a gas is high and the number of variables is significant,

is to use a statistical description with probability distributions. A distribution function f is defined as the density, in a six dimension phase space of coordinates, of all the variables represented as a point at a time instant t.

Considering $dN(\mathbf{r}, \mathbf{v}, t)$ as the number of points inside a volume element of $d\mathbf{r}d\mathbf{v}$, the distribution function can be defined as:

$$f(\mathbf{r}, \mathbf{v}, t) = \frac{dN(\mathbf{r}, \mathbf{v}, t)}{d\mathbf{r}d\mathbf{v}} \tag{2.5}$$

Since the distribution function is defined in a statistical way, its value defines a probable number of molecules, which can be elaborated to find the macroscopic properties of the gas.

For example, the gas velocity average value can be defined using this approach:

$$\mathbf{v}_h(\mathbf{r}, t) = \frac{1}{\rho(\mathbf{r}, t)} \int_{-\infty}^{\infty} mv \cdot f(\mathbf{r}, \mathbf{v}, t) d\mathbf{v} \tag{2.6}$$

where m is the mass of each particle.

To sum up, this procedure based on the distribution function gives the possibility to evaluate the average value of a variable as a function of position and time, because the integration is made considering the velocity space.

2.1.1 The Boltzmann Transport Equation

The Boltzmann transport equation (BTE) aims to describe the behavior of a dilute gas (where Euler and NS equations lose their validity) in thermal non-equilibrium using a statistical approach, starting from the distribution function f of a specific variable. External forces and internal collisions are taken into account. In this context, different assumptions are made to derive the equations:

- only binary collisions are considered since the gas density is assumed to be low.
- collisions are considered to be instantaneous, so collisions influence the velocity of the particles, without changing their position.
- the assumption of molecular chaos is made: collisions are considered as a random event, so they are treated using a statistical approach.

Starting from these assumptions, it is possible to extract the rate of change of particles inside the previously defined volume element $d\mathbf{r}d\mathbf{v}$:

$$\frac{\partial N}{\partial t} = \frac{\partial}{\partial t}(f d\mathbf{r} d\mathbf{v}) \tag{2.7}$$

The number of particles in the finite volume element changes because of intermolecular collisions and convection across $d\mathbf{r}$, $d\mathbf{v}$ caused by the molecules motion and acceleration by the external force. As a consequence of the provided assumptions, the BTE can be defined as follows:

$$\frac{\partial f}{\partial t} + \mathbf{v} \cdot \nabla_r f + \mathbf{a} \cdot \nabla_v f = \left(\frac{\partial f}{\partial t}\right)_c \tag{2.8}$$

In this equation, f is the distribution function previously defined, $\mathbf{v} \cdot \nabla_r f$ is the term related to the convective effect, $\mathbf{a} \cdot \nabla_v f$ is the diffusive term obtained through the force per unit mass independent from velocity and ∇ is the nabla operator which in this case, is defined in two different spaces as:

- position space: $\nabla_r = \left(\hat{x}\frac{\partial}{\partial x} + \hat{y}\frac{\partial}{\partial y} + \hat{z}\frac{\partial}{\partial z}\right)$
- velocity space: $\nabla_v = \left(\hat{x}\frac{\partial}{\partial v_x} + \hat{y}\frac{\partial}{\partial v_y} + \hat{z}\frac{\partial}{\partial v_z}\right)$

The term $\left(\frac{\partial f}{\partial t}\right)_c$ takes into account the effect of the collisions on the distribution function. If its value is 0, the Vlasov equation is defined and the gas is collisionless. If collisions are considered, the right hand of the equation is an integral depending on the properties of the collisions among particles and it is challenging to solve using both analytical and numerical methods.

Different methods have been proposed to solve the BTE: analytical methods require a particular family of distributions, typically unrealistic, to provide an exact answer to study the qualitative behavior of the solutions [20]; on the other side numerical methods provide good accuracy when simulating the complete physics of the flow or when discretizing the equation.

The most promising and used numerical methods are the ones that act on the physics of the flow because the Boltzmann equation is based on the study of the molecules motion, so a high number of degrees of freedom and points would be needed to represent the phase space to solve directly the BTE. Analyzing the physics of the flow allows to consider the particles directly and study their evolution in terms of position, speed, and internal state over time, while taking into account the molecular motion and intermolecular collisions in a deterministic way. DSMC falls in this class of methods.

In chapter 3 a complete outline of the DSMC method along with the software used to perform the simulations is shown.

2.2 Newtonian Theory

In this section, an overview of the Newtonian theory is given. Newton developed a theory in 1687 for low-speed fluid-dynamic applications, however, over the years it

has been disproved for this kind of use. The Newtonian theory became of interest when modern hypersonic aerodynamics developed, as a matter of fact, Newton's theory has been used to obtain a law to describe the force on an inclined plane located in a flow. The main assumptions associated with this theory are:

1) The linear or the translational motion of the molecules is taken into account, while the random movement is ignored, so the interaction between the molecules is neglected.

2) The stream of particles that hits the surface, transfers its normal momentum to the surface but saves the tangential component of the momentum, causing the particles to move tangentially to the surface.

3) Only the frontal area of the surface hit by the flow contributes to the impact pressure.

This latter assumption has made it possible to rename the Newtonian theory as "the Impact theory" since only the impacted areas of the surface by the flow influence the aerodynamics of the body. To derive the outcome of the current theory, assumption 2 comes into hand, in fact, the mass flow incident on a surface area A is defined as:

$$\dot{m} = \rho_\infty V_\infty A sin(\theta) \tag{2.9}$$

where ρ_∞ is the density of the flow, V_∞ is the free stream velocity and θ represents the angle of inclination of the surface with respect to the flow.

From Eq. 2.9 the time rate of change of normal momentum associated with the mass flux can be extracted and defined as the force acting on the whole surface:

$$F = \dot{m} \cdot V_\infty \cdot sin(\theta) = \rho_\infty V_\infty^2 A sin^2(\theta) \tag{2.10}$$

The normal force per unit area is then:

$$\frac{F}{A} = \rho_\infty V_\infty^2 sin^2(\theta) \tag{2.11}$$

The outcome of Eq. 2.11 represents the pressure difference between the surface pressure p and the stream static pressure p_∞. Moreover the free stream dynamic pressure can be defined:

$$q_\infty = \frac{1}{2}\rho_\infty V_\infty^2 \tag{2.12}$$

Hence, the pressure coefficient can be determined as:

$$\frac{F}{A} = p - p_\infty \Rightarrow C_p = \frac{p - p_\infty}{q_\infty} = 2sin^2(\theta) \tag{2.13}$$

Eq. 2.13 shows the final output of the Newtonian theory, this theory has great applicability when the Mach number is high [23] since the generated shock wave is

infinitesimally thin and situated near the body, neglecting any friction between the body and the shock layer.
A scheme for the considerations made on the Newtonian theory is shown in figure 2.3.

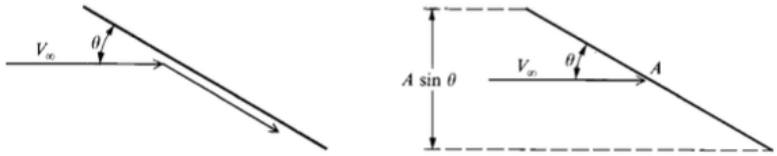

Figure 2.3: Scheme used for Newtonian theory [6].

Based on this review, the Newtonian theory is defined as a local surface inclination method where the pressure coefficient is a function of only the local surface inclination angle, and it is independent of the free stream speed and composition.

After further studies, a modification of the Newtonian theory has been proposed by Lees [30], this adjustment has shown a more accurate pressure distribution over blunt bodies and it is defined as:

$$C_p = C_{p,max} sin^2(\theta) \tag{2.14}$$

Where $C_{p,max}$ is the maximum pressure coefficient at the stagnation point, computed using the total pressure posterior to a normal shock wave, and it is a function of M_∞ and γ:

$$C_{p,max} = \frac{2}{\gamma M_\infty^2} \left\{ \left[\frac{(\gamma+1)^2 M_\infty^2}{4\gamma M_\infty^2 - 2(\gamma-1)} \right]^{\gamma/(\gamma-1)} \left[\frac{1-\gamma+2\gamma M_\infty^2}{\gamma+1} \right] - 1 \right\} \tag{2.15}$$

The pressure distribution defined in Eq 2.14 tends to the Newtonian theory outcome (Eq 2.13) as $M_\infty \to \infty$ and $\gamma \to 1$.

2.3 Aerodynamic Concepts

In this section, some basic aerodynamic concepts are introduced to complement the theories explained before.

The outcome sought from the methods explained before is the evaluation of the aerodynamic forces that act on the bodies exposed to a flow during the reentry. In particular, the velocity distribution around the body is researched to evaluate how the pressure spreads all over the object. The pressure distribution allows calculating the center of pressure location along with the aerodynamic forces

applied to it. The correlation between pressure and forces on an object composed by n surfaces is reported:

$$\mathbf{F} = \sum_{n} p\mathbf{n}A \tag{2.16}$$

In equation 2.16, A is the area of each infinitesimal surface, p is the pressure exerted on each surface by the flow and $\mathbf{n}$ is the normal direction to each surface.
Starting from this definition it is possible to extrapolate the drag and lift forces:

- Drag (D) is the force component parallel to the direction of the relative motion of the body.
- Lift (L) is the force component perpendicular to the direction of the relative motion of the body.

As explained before, these forces are applied in the center of pressure and they create a pitching moment when evaluating the moment with respect to a point different than the center of pressure. The moment is evaluated using the following equation:

$$\mathbf{M} = \mathbf{D} \times \mathbf{r}_d + \mathbf{L} \times \mathbf{r}_l \tag{2.17}$$

where $\mathbf{r}_d$ and $\mathbf{r}_l$ are respectively the distance between the point against which the moment is calculated and the drag and lift force application point.

A graphic representation of the forces applied on an airfoil is shown in figure 2.4.

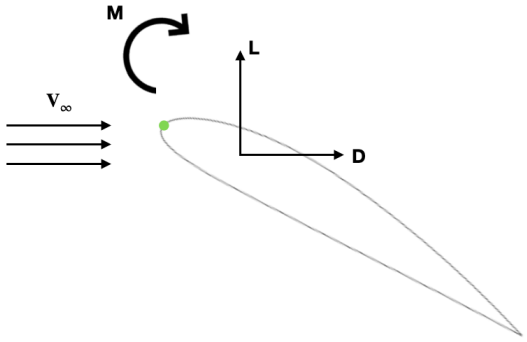

Figure 2.4: Schematization of lift, drag, and moment applied on an example airfoil. In green, is an example point against which the moment is evaluated.

To conclude, the aerodynamic coefficients are computed. By definition, they represent an adimensional quantity extracted from the integration of the pressure coefficients over the surface that shows the aerodynamic characteristics of the body

when exposed to a flow. The aerodynamic coefficients are obtained by normalizing the respective force/moment with the dynamic pressure of the flow. Their definition as used in this thesis for lift, drag, and moment is shown respectively in Eq. 2.18, 2.19, 2.20.

$$C_l = \frac{L}{\frac{1}{2}\rho V_\infty^2 S_{ref}} \tag{2.18}$$

$$C_d = \frac{D}{\frac{1}{2}\rho V_\infty^2 S_{ref}} \tag{2.19}$$

$$C_m = \frac{M}{\frac{1}{2}\rho V_\infty^2 S_{ref} l_{ref}} \tag{2.20}$$

In the above equations, ρ is the flow density, V_∞ is the free stream speed, S_{ref} is the reference surface that depends on where the cross-section is taken, while l_{ref} is the reference length considered to make the moment coefficient adimensional.

Chapter 3

Numerical Solvers and Methods

In this chapter, a description of the used codes combined with the methodology associated with them is provided. Three software have been taken into account to evaluate the aerodynamic coefficients of different objects during the re-entry: ANTARES is a Newtonian flow solver, SMARTA is a code based on the view-factor method and SPARTA is a DSMC code to solve low-density gas simulations.

3.1 ANTARES

ANTARES stands for "Application of Newtonian Theory for ARbitrary Entry Shapes". It is a MATLAB code based on the Newtonian theory for hypersonic flows during the re-entry for arbitrary objects, developed and validated by Thomas Durbin and Guillaume Grossir at VKI [18]. The code is composed of different tools implemented using MATLAB capabilities to set the simulations:

- **3D object handler**: this tool can read geometries in binary STL and ASCII STL formats; the geometries are then converted into a format readable by the code using faces and vertices. This tool also allows the rotation of the geometries with respect to the flow using Tait-Bryan angles [19], to speed up the analysis at different AOA configurations for the shapes.
- **Flow properties manager**: this instrument handles the properties of the flow that hits the body. It gives the possibility to set the fluid characteristics as the freestream Mach number, velocity, static pressure, and heat capacity ratio. These quantities are then used to compute the stagnation point maximum pressure coefficient using different approaches: Newtonian ($C_{p,max} = 2$), modified Newtonian ($C_{p,max}$ as a function of γ [6]), blunt bodies ($C_{p,max}$ as a function of γ, M_∞ - Eq. 2.15).
- **Calculation tool**: this instrument takes the elements described before as an input and computes the local pressure, force, and moments and the respective

aerodynamic coefficients normalized using the dynamic pressure and the reference surface. This tool starts by evaluating the normal vectors associated with each surface belonging to the shape to compute their orientation with respect to the flow, this helps in understanding which surfaces are exposed to the flow to evaluate their local pressure coefficient using Newtonian theory; the software is also able to detect shadowed surfaces in complex objects using projections, to estimate the contribution to the aerodynamic characteristics of the objects when some surfaces are not entirely revealed to the freestream. The aerodynamic forces and moments are calculated using an integration on all the surfaces in both body and inertial reference frame.

- **Visualization tool**: this instrument allows to display the aerodynamic results and the geometry attitude for each simulation both in MATLAB and Tecplot environment [5].

The usual limitations of the Newtonian theory are applied: shock interaction and concave surfaces provide inaccurate results. To sum up, the following steps are done by ANTARES to perform the simulations:

1) Geometry and flow properties are taken as input.

2) $C_{p,max}$ evaluation based on flux properties and selected approach.

3) Normal vectors outgoing of each surface ($\bar{n}$) computed.

4) The angle η between flow direction ($\bar{u}$) and each normal vector ($\bar{n}$) is evaluated.

5) Research of the maximum pressure point for the complete surface where the $C_{p,max}$ will be set.

6) C_p assignation to each surface element following modified Newtonian pressure distribution $C_p = C_{p,max} \cdot cos^2(\eta)$. The flow is seen as an isoentropic expansion starting from the stagnation point.

7) Pressure and forces computation for each surface and their subsequent integration:

$$p = p_{dyn} \cdot C_p + p_\infty \Rightarrow \mathbf{F} = -\mathbf{p} \cdot S,\ \mathbf{M} = \mathbf{F} \times \mathbf{R} \tag{3.1}$$

where $\mathbf{R}$ is the distance between each surface center of gravity and the point against which the moment is evaluated.

3.2 SMARTA

SMARTA is an open-source software developed at VKI by Pietro Parodi [2] to solve problems related to a collisionless gas that hits surfaces that reflect diffusively the gas. The solver takes advantage of the analogy between the equations that define the mass flow in a free molecular regime and the heat flux in a radiation problem; this similitude allows the development of a method able to solve free molecular problems reducing the computational cost without impacting the accuracy of the results.

The code is written in Python 3 and it is complemented using Message Passing Interface (MPI) to parallelize the workload and speed up the computation. The outcome of the software has been compared to analytic solutions and validated in the free molecular regime with maximum discrepancies lower than 0.2% [37].

Different studies in the past have tried to exploit the view factors between surfaces to solve free molecular problems [7] and some methods have been implemented to reduce the computational cost associated with free molecular simulations performed using DSMC [40], however, the view-factor method implemented in SMARTA allows to take into account the effects of a velocity with a drifting component.

3.2.1 View-Factor Based Method

The view factor method on which SMARTA is based is here described.

At the basis of the method, is the fact that it is applicable when the collisions between the surface and particles are fully diffusive, so the speed of the particles emitted by the surface is independent of the incident velocity: the scattered particles have a velocity obtained from a Gaussian distribution depending on the surface temperature. Moreover, the gas has to be in free molecular conditions, therefore the collisions among particles are less frequent than the collisions with the surfaces and the Knudsen number should be $Kn > 10$.

The view-factor method relies on the numerical computation of the view factor between two surfaces (F_{i-j}), it evaluates the fraction of energy from the emitting surface i that is exchanged with the surface j. This quantity depends solely on the reciprocate positioning of the considered surfaces, so it is dependent only on the geometric properties. The definition of the view factor among two surfaces is the following, obtained integrating on surface i:

$$F_{ij} = \frac{cos\theta_i cos\theta_j}{\pi s^2} A_j \tag{3.2}$$

where i, j are two infinitesimal surfaces of area A and θ is the angle between the normal unit vector of the surface ($\bar{n}$) and their distance s. In figure 3.1 all the quantities contained in Eq. 3.2 are shown.

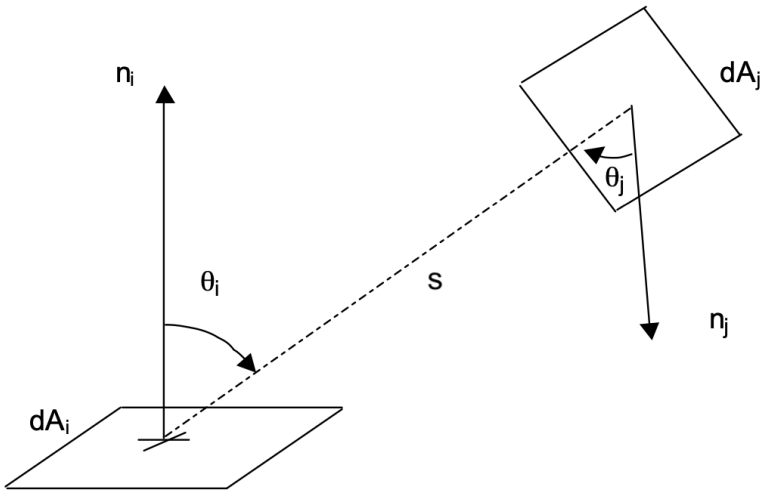

Figure 3.1: View factor between surfaces i and j - Adapted from [35].

The view factor value falls between $0 < F_{ij} < 1$, its value is 0 when the surfaces are not in any sight or an obstruction is present, while it is equal to 1 when they are fully exposed between each other. It is also worth noting that summing up all the view factors of a surface gives a unit value because the same amount of emitted radiation is absorbed as a consequence of the energy conservation principle. Moreover, a reciprocity principle applies so:

$$A_i F_{ij} = A_j F_{ji} \tag{3.3}$$

The view factors are evaluated using numerical methods such as the one used in SMARTA [22]. Once the view factors (F_{ij}) are computed, the parallelism between the heat flux in a radiation problem and the mass flux in a free molecular problem is applied to evaluate the number flux of particles from an emitting surface A_i, the resulting equation is reported here [37]:

$$\Phi_{i-j} = E_i F_{ij} M_{ij} \tag{3.4}$$

- F_{ij} are the view factors.
- E_i is the thermal mass flow.
- M_{ij} takes into account the contribution of the gas velocity.

The pressure on each surface is therefore evaluated:

$$\mathbf{p}_{i-j} = \Phi_{i-j}(m\mathbf{v}) \tag{3.5}$$

It is now necessary to add the effects of the momentum of the outcoming particles from the surfaces [12, 37]:

$$\mathbf{p}_i^{ex} = -\frac{1}{2} n K_b T \bar{\mathbf{n}}_\mathbf{i} \tag{3.6}$$

The final equation to evaluate the pressure on each surface is obtained:

$$\mathbf{p}_i = \sum_{j=1}^{N} \left(\mathbf{p}_{i-j} \frac{A_j}{A_i} \right) + \mathbf{p}_i^{ex} \tag{3.7}$$

The equations are distributed into matrices to create a linear system. The aerodynamic forces (Eq. 3.8) and moments (Eq. 3.9) associated with the problem are computed using the following equations:

$$\mathbf{F}_i = \mathbf{p}_i A_i \tag{3.8}$$

$$\mathbf{M}_i = \mathbf{F}_i \times \mathbf{r}_i \tag{3.9}$$

where $\mathbf{r}_i$ is the distance between the surface and the point against which the moment is calculated.

3.2.2 SMARTA Software

A brief overview of SMARTA and the sequence of actions to perform a run is described here. SMARTA will be defined as the free molecular code since it has been validated in this aerodynamic regime. During a simulation the following steps are undertaken:

1) The complete mesh is loaded and divided as a source (which emits particles) and a wall (which reflects diffusively).

2) The source flow properties and the surface temperature are set and initialized. The code takes as an input the atmospheric properties (p, T, n, m) and the velocity properties of the flow in terms of magnitude and direction.
The magnitude of the flow speed is defined using the speed ratio as follows:

$$S = \sqrt{\frac{\gamma}{2}} M_\infty \tag{3.10}$$

3) The computation of the view factors between the surfaces is done as previously explained.

4) Solution of the linear system of equations is performed using matrices through Python NumPy library.

5) The total flux, the total pressure distribution, and the aerodynamic forces and moments, are evaluated by integrating over all the surfaces following the theory explained above.

6) The aerodynamic forces and moments are shown in a Linux terminal window, while all the quantities distributions are accessible through ParaView.

The described code provides a faster way than DSMC to study free molecular problems, the computational cost depends on the number of surface elements to analyze, since most of the time of a simulation is related to the computation of the view factors. In particular, the computational weight and time increase with the second power of the number of surfaces analyzed $O(N^2)$. To conclude, it is worth saying that the code can save the view factors related to a particular problem, so if a change in the boundary conditions associated with the flow is needed, it is possible to run the simulation without having to evaluate all the view factors again, but just solving the linear system with the new inputs, saving most of the required computational time.

3.3 SPARTA

SPARTA (Stochastic PArallel Rarefied-gas Time-accurate Analyzer) is an open-source code developed by M. A. Gallis and S. J. Plimpton at Sandia National Laboratories [3]. The code is based on the Direct Simulation Monte Carlo method elaborated by G. A. Bird [11] to solve rarefied gas problems in a transitional regime.

3.3.1 Direct Simulation Monte Carlo Method

DSMC is a particle method belonging to the class of physics-based methods. It is one of the preferred techniques to simulate gases in thermal non-equilibrium since it works by defining directly each particle motion, distributed uniformly over the domain, using a Maxwellian distribution. This means that this method has a stochastic nature and the results could be affected by a statistical error. The objective of DSMC is to simulate the dynamics of a gas without directly solving the BTE, the latter is a non-linear equation in 7 variables (3 positions, 3 velocities, and time), so the discretization on a grid of the distribution function arguments could be computationally heavy. The main elements of the DSMC method are the cell size in the grid, the timestep used for the simulations, and the number of simulated particles.

- **The grid** associated with the domain has to resolve the local mean free path in every direction and the gas properties have to be as uniform as possible during the simulation in each cell to simulate a realistic condition.

- **The timestep (Δt)** used in the simulations represents the time in which the motion of the particles is considered, the position of each particle is updated every timestep until the final simulation time is reached. This parameter

is important because it has to be selected to allow the decoupling of the particle's motion and collisions in the flow, so its value has to be lower than the mean collision time among molecules (τ_{coll}) defined as:

$$\tau_{coll} = \frac{\lambda}{v_{th}} \tag{3.11}$$

where λ is the local mean free path and v_{th} is the thermal velocity of the gas defined as the average molecular speed:

$$v_{th} = \sqrt{\frac{8K_bT}{\pi m}} \tag{3.12}$$

Using these considerations it is also possible to simulate a flow where each particle does not cross more than one cell for each timestep.

- **The number of simulated particles (N_{part})** represents the number of simulated molecules in the domain, it directly impacts the accuracy of DSMC, so it is important to have a high number of particles to reduce the statistical error built-in the method defined as:

$$standard\ error \sim \frac{1}{\sqrt{N_{part}}} \tag{3.13}$$

Moreover, it is necessary to have a sufficient number of particles in each grid cell to reduce the error on the selected collision rate, therefore it is recommended to fill each cell with as many particles as possible. Increasing the number of particles causes a rise in the computational cost because the number of binary collisions drastically increases, so a compromise has been found in using around 20 particles per cell to obtain a good accuracy in the results [10].

The DSMC scheme showing the procedure for the simulations is displayed in figure 3.2.

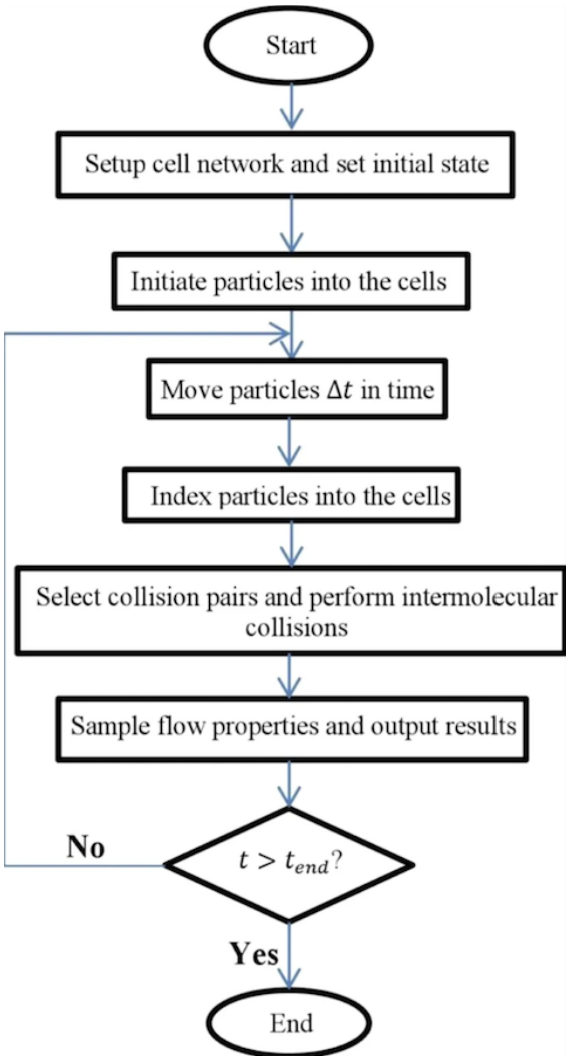

Figure 3.2: DSMC procedure flow chart [41].

The starting phase of a DSMC simulation is always a transient stage to reach the steady state conditions in the domain. After reaching the steady state, the collisions between particles are performed stochastically to propagate their speed and trajectories in the domain, then the properties are sampled and averaged; the sampling is performed over different timesteps to reduce the statistical error. In addition to the standard error, a numerical error is also introduced in the simulations, the latter is due to the space and time discretization and cannot be controlled in advance of the run, so a convergence study is needed to reduce the error.

To sum up, the computational cost of DSMC is proportional to the number of simulated particles; the number of collisions is proportional to the number density (n) times the number of particles in each cell, and since the flow number density does not change, the parameter that affects the number of collisions is n. Moreover,

DSMC provides an accuracy of the first order on both the spatial grid size and time since a forward Euler integration is used.

For the performed analysis, DSMC has been chosen as the reference method since the flow regime falls in between free molecular and transitional, so the gas is considered dilute.

3.3.2 SPARTA Software

A description of the SPARTA software is shown in this section.

To reduce the high computational cost associated with DSMC, SPARTA is able to work on single-processor machines or on shared-memory parallel machines to perform simulations of low-density gas in both 2D and 3D using the MPI library. The code is written in C++ and it is able to solve complex problems taking into account collisions, chemistry, and boundary conditions using a hierarchical Cartesian grid to solve the Boltzmann equation (Eq. 2.8).

Cartesian Grid

SPARTA generates a hierarchical Cartesian grid in the simulation domain to track particles in the same grid cell and execute collision and chemistry operations among them. The use of a hierarchical grid makes it possible to split the grid cells into smaller cells iteratively, to refine the grid and obtain a uniform distribution of particles in the grid cells. The grid is wrapped around the solid objects readable by SPARTA in 2D (line-segmented surfaces) or 3D (triangulated surfaces); each surface is assigned to the grid cells that intercept to make possible the analysis of the particle-surface interactions. SPARTA also allows performing an adaptive grid refinement during the simulation, with the aim of adjusting the cell size to a particular attribute (i.e. mean free path, the number density of particles).

The grids used in the analyses are bidimensional since the performed simulations are 2D, so the particle motion develops in the xy plane; however, to compute the properties of the flow, all the three components (x,y,z) for each quantity have to be evaluated.

Surface Collisions

SPARTA uses the model provided by Maxwell to analyze the interaction between particles and surfaces. This model uses the accommodation coefficient to evaluate how the speed and trajectory of a molecule that hits the surface evolves. The accommodation coefficient is defined in Eq. 3.14.

$$\alpha = \frac{E_i - E_r}{E_i - E_w} \tag{3.14}$$

where E_i is the energy of the impacting particles, E_r is the energy associated with the reflected particles and E_w is the energy associated with the reflected particles

if the gas would be in thermal equilibrium with the wall.

This coefficient defines the fraction of energy exchanged by the gas with the wall, over the maximum exchangeable energy. Its value is between 0 and 1:

- if $\alpha = 1$ the surface is fully diffusive. This kind of interaction produces a change in the speed of the particle following a Maxwellian velocity distribution depending on the local surface temperature, so the post-interaction speed is evaluated using thermal equilibrium between speed direction and local temperature. The surface is considered rough and the accommodation coefficient depends on the fluid and the properties of the wall.
- if $\alpha = 0$ the surface is fully specular. This scenario occurs when a perfectly smooth surface is considered and a perfectly elastic collision happens. The speed of the particles stays the same in magnitude, while the speed normal direction to the surface is inverted; that takes place because no energy exchange occurs, so the scattering angle is the same as the incident angle.

To set the collisions between particles and surfaces, SPARTA only needs the type of collision along with the accommodation coefficient value and the surface temperature. A representation of the aforementioned types of collision is shown in figure 3.3.

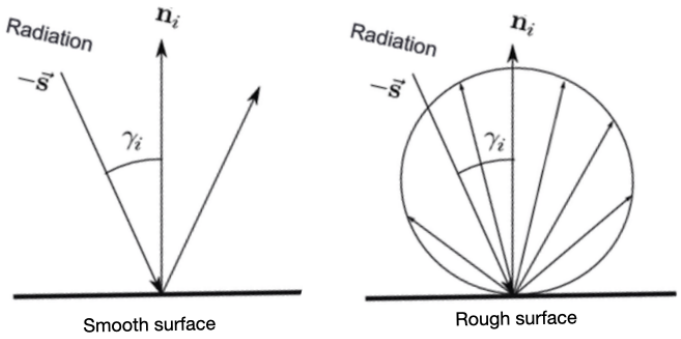

(a) *Fully specular interaction* (b) *Fully diffusive interaction*

Figure 3.3: Surface-gas interaction model - Adapted from [31].

Gas Phase Collisions

To improve the realism and accuracy of the analyses, SPARTA implements different molecular interaction models to represent the particles based on the cross-section and the scattering angle of each molecule.

The collision cross-section (σ) is defined as the area around a molecule in which the center of another particle must be, to make a collision happen.

The scattering angle (χ) represents the angle at which the particle will be dispersed after the collision occurs.

A basic representation of an elastic collision is shown in figure 3.4.

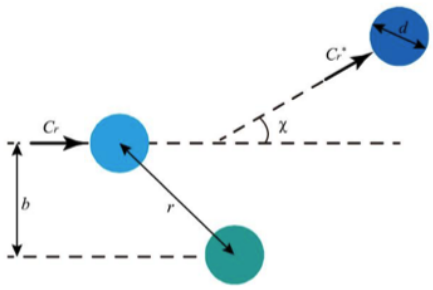

Figure 3.4: Elastic collision example [16].

3 different molecular interaction models are implemented in SPARTA:

- The Hard-Sphere Model (HS) is the simplest model to simulate a rarefied gas, in this case, the scattering angle is isotropic and the collision cross section is constant. The definition of σ and χ for the HS model is shown in Eq. 3.15, 3.16:

$$\sigma = \pi d^2 \tag{3.15}$$

$$\chi = 2cos\left(\frac{b}{d}\right) \tag{3.16}$$

  where d is the distance between the center of the molecules. This model is not usually adopted since the collision cross-section is independent of the relative speed between the particles and so of the translational energy.

- The Variable Hard-Sphere Model (VHS) was proposed by Bird to improve the simplification of the HS model. In this case, the cross-section is dependent on the relative velocity between the molecules as shown in Eq. 3.17, while the scattering angle is still considered isotropic and so equally possible in all the directions as in the HS model.

$$d = d_{ref}\left(\frac{\|v_r\|}{\|v_r\|_{ref}}\right)^{-\eta} \tag{3.17}$$

  Where d_{ref} is a molecule reference diameter and v_r represents the impacting particle speed. This model is however incomplete since the diffusion coefficients sometimes disagree with experimental results.

- The Variable Soft-Sphere Model (VSS) was implemented by Koura and Matsumoto to consider the scattering angle anisotropic and dependent by a parameter α. This parameter makes it possible to match the self-diffusion coefficient of a gas and its viscosity. The collision cross-section is defined as follows:

$$d = 2arccos\left(\frac{b}{d}\right)^{1/\alpha} \tag{3.18}$$

  The VSS model is able to combine the simplicity of the VHS model with accurate modeling of the mass diffusion in a gas mixture, so it is the adopted model in DSMC simulations.

SPARTA can also compute elastic and inelastic collisions between particles following the Borgnakke-Larsen model which is able to evaluate the collisions based on discrete energy levels. In particular:

- Elastic collisions happen when there is no exchange of vibrational and rotational energy among the particles and the total energy is the same after the collision; in this case, the molecules are considered monoatomic species.

- Anelastic collisions occur when there is an exchange between vibrational and rotational energy among the particles, but the total momentum stays constant. The post-collision translational and rotational energies are computed from a Maxwellian equilibrium distribution.

To evaluate the collisions among particles, SPARTA uses the No-Time-Counter (NTC) algorithm which imposes a maximum number of collisions in a cell during a timestep. The algorithm then selects pair of particles on which to perform collisions depending on the selected timestep. When the pairs are selected, an acceptance-rejection method is applied to see if the collision is accepted based on the cross-section and the relative speed among the particles.

In addition to the gas and surface collisions, it is also worth pointing out that SPARTA is able to compute the chemistry between molecules when ionization, dissociation, exchange, and recombination happen for both gas phase and surface reactions.

Chapter 4

Test Case Definition

In this chapter, the structure of the simulations summarized in chapter 5 is introduced. First of all, the basic assumptions are issued, then the selected geometries to perform the analyses are shown; to conclude, an overview of the software input is illustrated. The main assumptions for all the simulations are:

- The considered flow is completely hypersonic in all the simulations (M>16) and the perfect gas model is used.

- Preliminarily, no atmospheric model has been considered. To make the codes comparable, the flow is made up of pure nitrogen N_2, considering a heat capacity ratio $\gamma = 1.4$, a specific gas constant $R = 296.8\frac{J}{kg \cdot K}$ and a molecular mass $m = 4.65e - 26\ kg$.

- The DSMC simulations have been performed in a 2D domain to lower the computational cost of the analyses.

- The aerodynamic coefficients evaluated in SMARTA and ANTARES have been rescaled to match the 2D analysis obtained using DSMC.

- Since the analysis are rescaled in 2D, only 3 coefficients have been evaluated: C_d is the drag force coefficient, evaluated in the parallel direction to the flow; C_l is the lift force coefficient, evaluated using the force perpendicular to the flow; C_m is the moment coefficient, evaluated in the plane containing the aforementioned lift and drag forces.

4.1 Shapes Selection

In this section, the reasons behind the selection of the studied shapes are explained. All the 3D shapes for SMARTA and ANTARES simulations have been modeled using the element mesh generator Gmsh [21]. On the other hand, all the 2D meshes

for the DSMC analyses have been created using MATLAB scripts to follow the convention needed by the command read_surf used in SPARTA.

4.1.1 C-Shape

This object has been selected since it recalls the shape of a simple reservoir for a space application. Moreover, this shape is useful to better understand the differences between the codes outside the free molecular flow approximation, since it has both a convex and a concave area where the particles pile up when it is exposed to the flux and the collisions between particles may create bigger discrepancies between the software.

2D geometry
The 2D geometry is characterized by an external diameter of 50 mm and an internal diameter of 46 mm. Consequently, the reference length used for the aerodynamic coefficients is 50 mm, which represents the maximum object length that can possibly be exposed to the flux. The surface mesh used for the 2D analyses is made up of 62 lines and it is shown in figure 4.1.

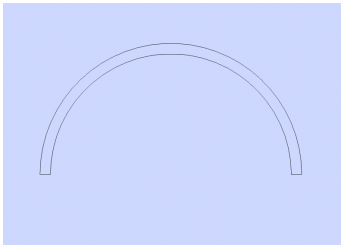

Figure 4.1: C-Shape 2D geometry.

3D geometry
As explained before, the 3D geometry is needed for SMARTA and ANTARES analyses, since they both read STL files. The 3D mesh is composed of 6128 triangles as shown in figure 4.2. It has the same dimensions used for the 2D geometry while having a 100 mm extrusion in the third dimension, so the reference surface used for the aerodynamic coefficients estimation is $S_{ref} = D_{ext} \cdot length = 0.005\ m^2$. It is worth saying that the number of lines that build the lateral section is the same as the 2D mesh, to make the geometries coherent as can be seen from figure 4.2(b).

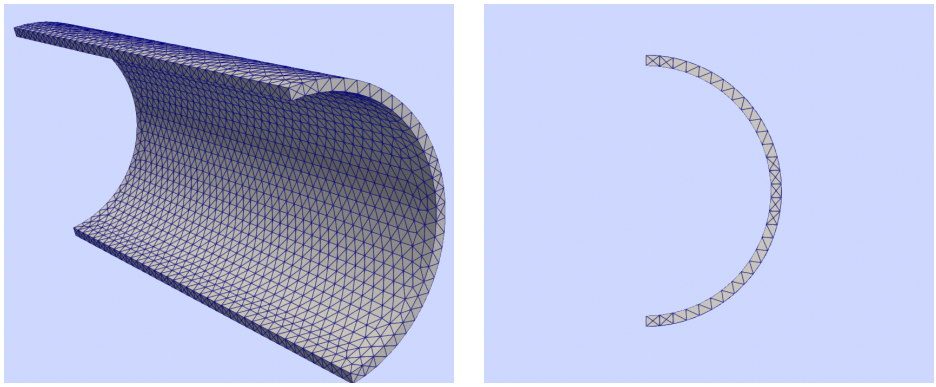

(a) *Ortographic view* (b) *Lateral view*

Figure 4.2: C-Shape 3D geometry.

4.1.2 Flat Plate

This shape has been picked due to the fact that it represents the solar panel of a satellite, therefore it is a typical shape that can be encountered in DSMCFED during re-entry analysis.

2D geometry
The 2D geometry is composed by 62 lines. The thickness of the flat plate is 2 mm, while its length is 0.1 m, to resemble as much as possible the dimensions of a solar panel equipped on a satellite. The reference length used for the calculation of the aerodynamic coefficients is 0.1 m, which is the maximum portion of the shape that can be exposed to the flux. The surface mesh is shown in figure 4.3.

Figure 4.3: Flat plate 2D geometry.

3D geometry
The 3D geometry has the same size as the 2D shape, but it is extruded in the third dimension for 100 mm as shown in figure 4.4. The considered reference surface is $S_{ref} = l_{ref} \cdot length = 0.01\ m^2$. It is worth pointing out that the number of triangles that make up the 3D mesh is 5600 and the number of lines that constitute the lateral section is the same as the 2D mesh.

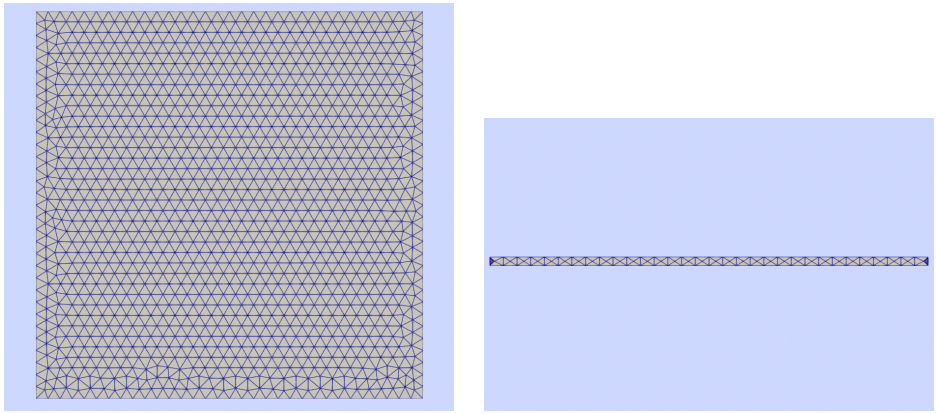

(a) *Frontal view* (b) *Lateral view*

Figure 4.4: Flat plate 3D geometry.

4.1.3 QARMAN Lite

This geometry has been chosen since it recalls the shape of the QARMAN platform developed by VKI. It has a simplified configuration where the solar panels (0.3 m x 0.1 m x 0.002 m) are perpendicular to the main body of the satellite, which is a 3U CubeSat (0.34 m x 0.1 m x 0.1 m).

2D geometry
The 2D geometry is shown in figure 4.5 and it is composed of 328 lines, the reference length used for the evaluation of the aerodynamic coefficients is 0.7 m, which represents the maximum length exposed to the flow in the 2D analyses.

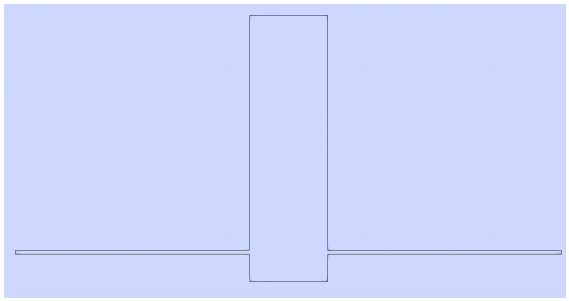

Figure 4.5: QARMAN Lite 2D geometry.

3D geometry
The 3D geometry features the same dimensions as the 2D one, while it has a 0.1 m extrusion in the third dimension. The surface mesh shown in figure 4.6 is composed

of 22626 triangles and the lateral section has the same number of lines as in the 2D mesh. The reference surface is $S_{ref} = l_{ref} \cdot length = 0.07\ m^2$.

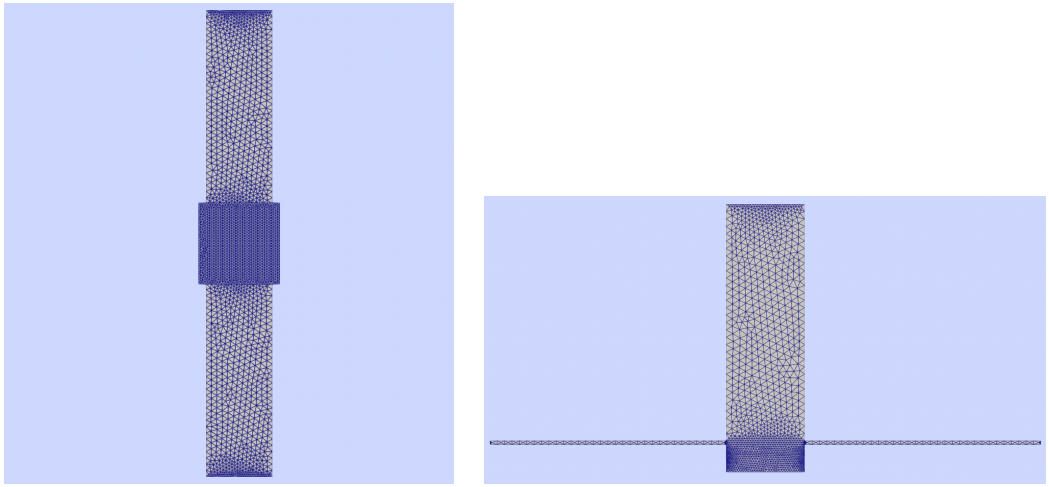

(a) *Frontal view* (b) *Lateral view*

Figure 4.6: QARMAN Lite 3D geometry.

4.2 Mach and Altitude Range

In this section, the flow conditions used in the simulations are presented, the atmospheric data are taken from [1], considering mean solar activity conditions.

Altitude Range
The selection of the altitudes to perform the simulations has been based on the flow Knudsen number, to cover different flow regimes and see how the comparison among the different codes evolves. Following what has been discussed in chapter 2 about the Knudsen number and the associated flow regime, and considering that DSMC analyses have been usually applied in the transitional regime, 3 different altitudes have been selected:

- 140 km: this altitude has been picked since the results between DSMC and SMARTA should be similar in the free molecular flow regime, therefore it was used as a validation means to check that the input of the different software were correctly set up. The atmospheric properties at this altitude are shown in table 4.1:

MFP [m]	T [K]	p [Pa]	n [$1/m^3$]	c [m/s]
21.204	635.57	7.03e-4	8.01517e+16	505.3

Table 4.1: Atmospheric properties used at 140 km.

- 100 km: this altitude has been selected since it falls in the range of the transitional regime, where the effect of the collisions between particles is relevant and the DSMC simulations start to become computationally heavy. The atmospheric conditions at this altitude are reported in table 4.2:

MFP [m]	T [K]	p [Pa]	n [$1/m^3$]	c [m/s]
0.1536	184.02	2.81e-2	1.1065e+19	271.9

Table 4.2: Atmospheric properties used at 100 km.

- 80 km: the last selected altitude was set at 80 km, this decision has been made after analyzing the Knudsen number of all the simulation cases, to perform analysis in the lower area of the transitional regime just before the flow falls in the continuum region. As pointed out in [32], DSMC analysis are less used than CFD when a low Knudsen number is simulated because the computational cost becomes too high. The atmospheric properties at 80 km are shown in table 4.3:

MFP [m]	T [K]	p [Pa]	n [$1/m^3$]	c [m/s]
4.873e-3	196.36	0.945	3.487e+20	280.8

Table 4.3: Atmospheric properties used at 80 km.

Mach Range
The Mach number range has been selected to cover different scenarios during the re-entry trajectory of typical debris. In particular, considering the set of altitudes selected, [13] shows that the Mach range for a sample re-entry capsule is between 20 and 40. Moreover, following the remarks made on the typical Mach range for the Space Shuttle during the re-entry trajectory [4], the identified Mach numbers for the simulations are 16-22-28, which fall in the range described above.

4.3 ANTARES Modelling

In this section, the modelization of the ANTARES analysis is shown. To set up the ANTARES runs, it was necessary to import the geometries described before in the STL format and provide the aforementioned reference surface and length. Then the surfaces were brought to the reference starting attitude from which the geometry was rotated autonomously by the code, to perform the simulations with different AOA configurations. The only parameters that could be set were the ones relative to the flow composition and conditions, along with the stagnation point

pressure coefficient. As explained before the selected gas was N_2, and the flow conditions are shown in section 4.2 for each altitude. To finalize the settings, the assigned maximum pressure coefficient was extrapolated from the DSMC analysis at each attitude, since the approximation provided by the Newtonian theory was deemed insufficient due to the strong simplifications. The resulting aerodynamic coefficients were directly provided by the code in tabular format, along with the pressure distribution on the surface for each analyzed configuration as shown in figure 4.7.

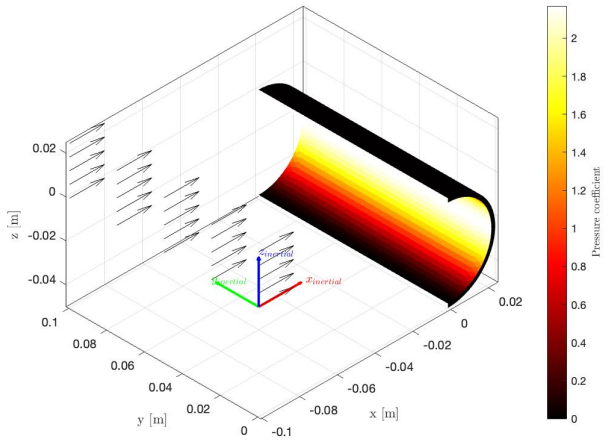

Figure 4.7: Example of the pressure distribution on the surface provided by ANTARES for the C-Shape at 90° AOA.

4.4 SMARTA Modelling

In this section, the modeling of the SMARTA analyses is explained. The preparation of the analyses started by providing the source and the object meshes to the code. The object is set as a wall since it reflects diffusely the particles by which it is hit, while the source is the mesh from which the particles belonging to the flow are emitted, it is important to have a source whose dimensions are much bigger than the object, in order to compute the view-factors among the surfaces in the correct way. The next step is to assign the properties to the surface groups, to simulate the flow conditions explained before. The studied object has only the surface temperature as an input parameter, the latter is set equal to the flow temperature at the simulated altitude. On the other side, the source parameters are multiple and are defined in section 4.2:

- Temperature [K].

- Number density of the gas in the reservoir $[1/m^3]$.
- Molecular mass of the gas in the simulation [kg].
- Velocity vector of the gas in the reservoir: always set in x direction.
- Speed Ratio (defined in section 3.2.2).

	Mach 16	Mach 22	Mach 28
Speed Ratio	13.387	18.406	23.426

Table 4.4: Speed ratio for the considered Mach numbers.

To conclude the settings of the simulations, the software also allows the computation of the moments with respect to a reference point set by the user. The forces and the moments are shown in a Linux terminal window from which they are extracted and normalized to obtain the aerodynamic coefficients as explained in section 2.3. An example of the SMARTA source and surface is shown in figure 4.8.

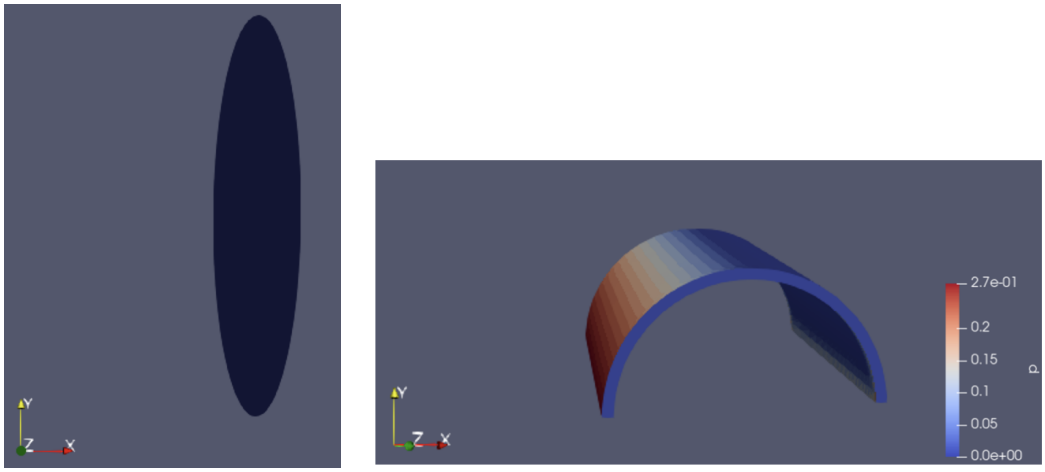

(a) *Circular source emitting in x positive direction*

(b) *C-Shape surface pressure distribution*

Figure 4.8: Example of the pressure distribution on the surface provided by SMARTA for the C-Shape at 0° AOA.

4.5 DSMC Modelling

In this section, the steps taken for modeling the SPARTA simulations are described. The modelization has been performed following the DSMC best practices [8] to optimize the results of the analyses in terms of statistical and numerical error. The following considerations have been applied:

- The number of particles considered in each simulation is sized according to the free stream to have approximately 20 particles per domain cell (n). To dimension this parameter, F_{num} was defined as:

$$F_{num} = \frac{n \cdot A_{sim}}{n_{sim}} \tag{4.1}$$

  In equation 4.1, n_{sim} is the number of simulated particles and A_{sim} is the area of the 2D domain.

- The area of the domain has been sized considering the dimensions of the object, to contain at least 3 times the shape in each direction and to solve the relative MFP; that allows seeing how the macroscopic fields evolve around the body and reduce the computational cost. In addition, the simulation box features open boundary conditions in each of the 2D dimensions (xy), while periodic conditions have been set along z.

- The grid size is dimensioned to resolve the MFP of the simulation, in particular, the dimension of the cells in each direction is defined as:

$$\Delta x \approx \frac{MFP}{5} \tag{4.2}$$

  To reach the condition mentioned in equation 4.2, firstly a static grid has been created to avoid each cell crossing more than one line of the mesh using the adapt_grid command, then a dynamic adapting has been performed on the local MFP to reach the requirement on the size and the number of particles in each cell.

- The timestep of the simulation is sized according to the time among the particle collisions in each cell (section 2.1). Particularly, the objective is to decouple free advection and collisions between particles, to do so, the timestep is defined as:

$$\Delta t \approx \frac{\tau_{coll}}{5} \tag{4.3}$$

- The gas composition and its properties have been set using the mixture command. In particular, to set the different AOA configurations, the flow has been rotated around the body, to prevent the static grid from changing for each new simulation.

- The collisions between particles have been modeled using the VSS model described in section 3.3 and the accommodation coefficient value has been set to 1, to make the SMARTA and SPARTA analyses comparable.

- Each simulation has been performed using 30000 timesteps as transient, while 100000 timesteps have been simulated after steady-state is reached.

- Each physical property, as forces and the macroscopic quantities in the domain, is evaluated every 100 timesteps in the steady-state phase of the simulations while accumulating the average value of each variable continuously.

An example of the grid for the C-Shape at 80 km altitude is shown in figure 4.9.

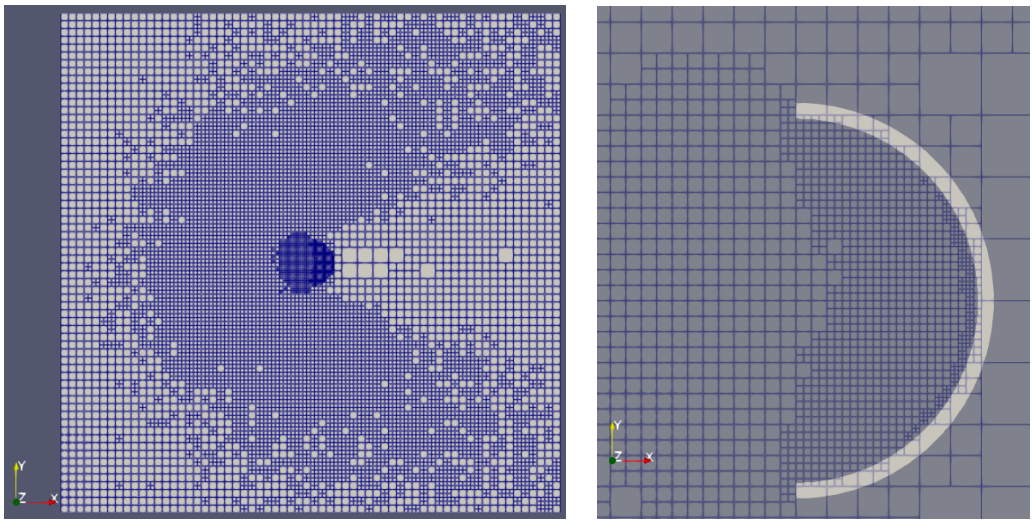

(a) *Full grid view* (b) *Zoomed grid view*

Figure 4.9: Grid definition in SPARTA for the C-Shape at 80 km altitude, Mach 16 and AOA=90° (flow in x positive direction).

Chapter 5

Numerical Simulations

As indicated in the first chapter, the objective of this work is to compare DSMC results with other codes to find out if it is possible to approximate the variation of the aerodynamic coefficients with respect to the attitude, starting from a single DSMC simulation while using lower fidelity software. This approach is used to seek a significant reduction in the computational cost of the simulations while accepting errors in the estimation. The objective of this chapter is to first show the outcome of the simulations for the different shapes analyzed, then all the results are summarized with the aim of creating an algorithm to make the final selection of the reference point to perform the starting DSMC run and minimize the errors for the coefficients approximation.

To evaluate the quality of the approximation with respect to DSMC results, the normalized root mean square error (NRMSE) has been examined. The selection of this parameter has been done to discard one of the two lower-fidelity codes to estimate the DSMC results and to see how the error propagates while the input change. The NRMSE is defined as in equation 5.1:

$$RMSE = \sqrt{\frac{1}{n}\sum_{i=1}^{n}(\hat{y}_i - y_i)^2} \rightarrow NRMSE = \frac{RMSE}{max\ y_i - min\ y_i} \tag{5.1}$$

In the above equation, n stands for the number of samples, $\hat{y}_i$ represent the predicted values calculated using SMARTA and ANTARES, while y_i are the reference values measured with SPARTA.

In [14], a complete overview of the root mean square error (RMSE) is done, and it points out that it could become inaccurate when the number of samples is lower than 10, however, this is the selected parameter to examine since it offers a full vision of the error distribution when the boundary conditions change. To overcome the limits imposed by the number of samples that can lead to inaccurate results [42], the NRMSE has been selected as the main criteria to make a preliminary choice on the more appropriate tool to compare the DSMC results.

5.1 C-Shape Results

The results in this section are referred to the object described in 4.1.1. The analyses are performed on the 3 available codes: SPARTA, SMARTA, and ANTARES; to evaluate if they produce comparable results in terms of drag, lift and moment coefficient in the different scenarios selected for the simulations. The runs are done for 9 different AOA with the convention shown in figure 5.1, while the moment is evaluated with respect to the first point of the mesh, indicated with a green dot.

AOA	-90°	-60°	-45°	-30°	0°	30°	45°	60°	90°

Table 5.1: AOA considered in the C-Shape simulations.

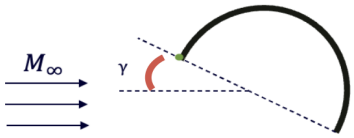

Figure 5.1: C-Shape geometry. The AOA (γ) is positive when the cavity is exposed to the free stream. The green dot represents the point around which the moment is evaluated.

5.1.1 Case: 140 km Altitude

The simulation parameters used for ANTARES and SMARTA are respectively shown in sections 4.3 and 4.4, while the parameters used for the SPARTA simulation are given in table 5.2. At an altitude of 140 km, the global Knudsen number is at its lowest value when the considered reference length is maximum, that happens when the angle of attack is 90° and the cavity is fully exposed to the flux. In this instance, the Knudsen number is:

$$Kn = \frac{\lambda}{l_{ref}} = 424.1$$

This case falls within the hypothesis of the free molecular flow regime, so the effect of collisions between particles is negligible. The runs performed at 140 km are carried out for every shape as a means of validation between SMARTA and SPARTA since their outcome should be equal in the free molecular flow regime. Figure 5.2 shows the results for C_d, C_l and C_m of the C-Shape for this test case.

	Simulation Data	Unit
Particles density	8.0152e+16	$[1/m^3]$
F_{num}	1.12e+15	-
Δt_{sim}	5.99e-5	[s]
Number of particles	200000	-

Table 5.2: C-Shape DSMC parameters at 140 km.

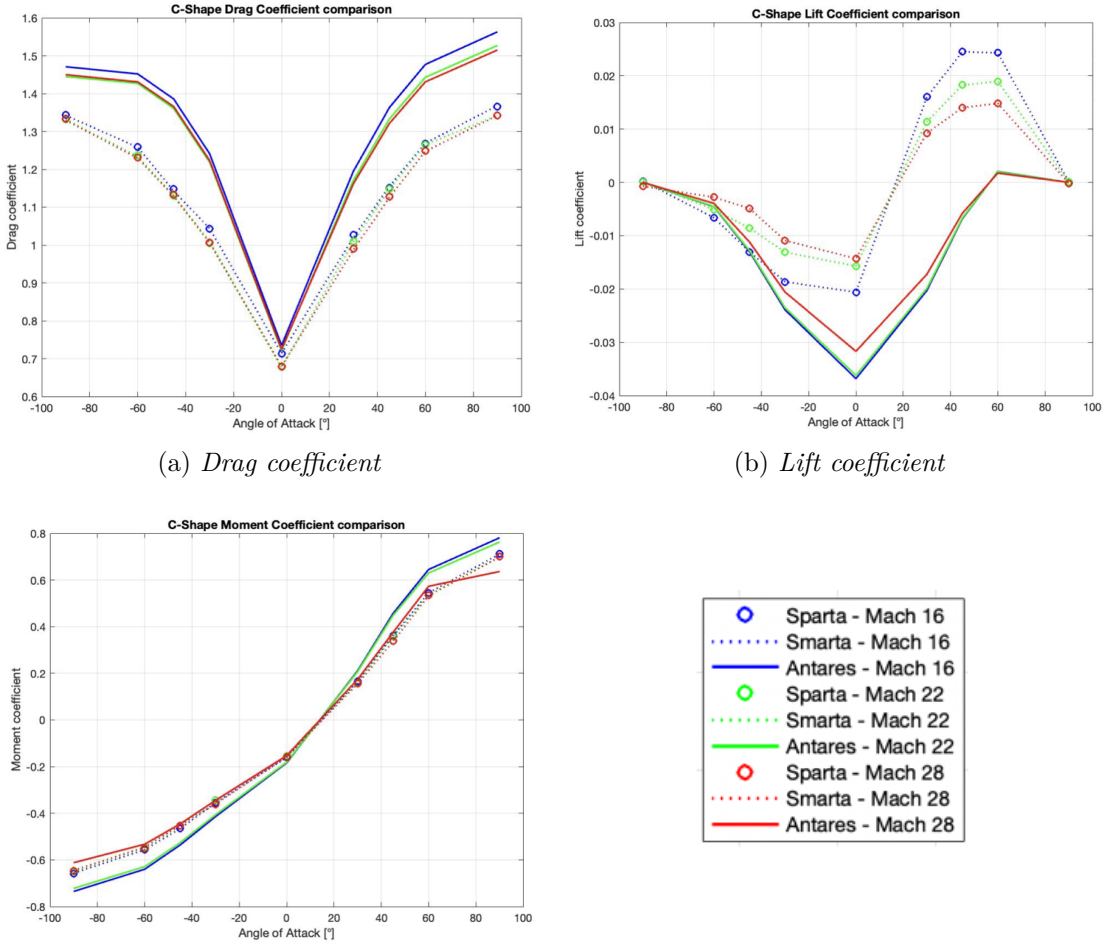

(a) *Drag coefficient*

(b) *Lift coefficient*

(c) *Moment coefficient*

(d) *Legend*

Figure 5.2: C-Shape aerodynamic coefficients results comparison - 140 km.

Tables 5.3, 5.4 display the normalized root mean square errors (NRMSE) considering DSMC results as a reference.

It is possible to see that the relative error between SPARTA and SMARTA is

NRMSE	Mach 16	Mach 22	Mach 28
C_d	0.56%	0.29%	0.21%
C_l	0.14%	0.06%	0.05%
C_m	0.51%	0.22%	0.19%

Table 5.3: SMARTA Normalized root mean square error - 140 km.

NRMSE	Mach 16	Mach 22	Mach 28
C_d	9.96%	8.54%	8.61%
C_l	32.8%	34.5%	33.1%
C_m	5.63%	5.55%	3.29%

Table 5.4: ANTARES Normalized root mean square error - 140 km.

extremely low over all the angles of attack for the 3 coefficients as expected and it is purely due to the statistical nature of DSMC. On the other side, the estimation produced by ANTARES is acceptable in terms of drag and moment coefficient, while it goes off with the lift coefficient especially when the cavity of the object is exposed to the flux. The reasons behind the inconsistency of ANTARES can be found in the Newtonian theory on which the software is based.

5.1.2 Case: 100 km Altitude

The simulations performed at 100 km fall in the transitional regime, in fact the global Knudsen number in this set of simulations is:

$$Kn = \frac{\lambda}{l_{ref}} = [3.072 \div 6.144]$$

Being in the transitional regime means that the approximation of the coefficients from SMARTA and ANTARES will be less accurate because they do not take into account the effect of collisions between particles. DSMC parameters for this set of simulations are reported in table 5.5.

	Simulation Data	Unit
Particles density	1.1065e+19	$[1/m^3]$
F_{num}	1.264e+14	-
Δt_{sim}	1.41e-6	[s]
Number of particles	350000	-

Table 5.5: C-Shape DSMC parameters at 100 km.

In figure 5.3, the comparison between C_d, C_l and C_m of the C-Shape at 100 km altitude is illustrated.

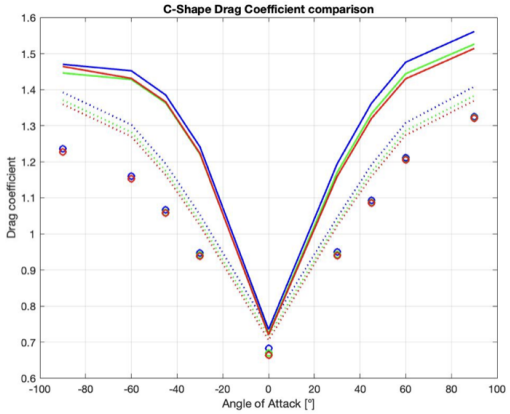

(a) *Drag coefficient*

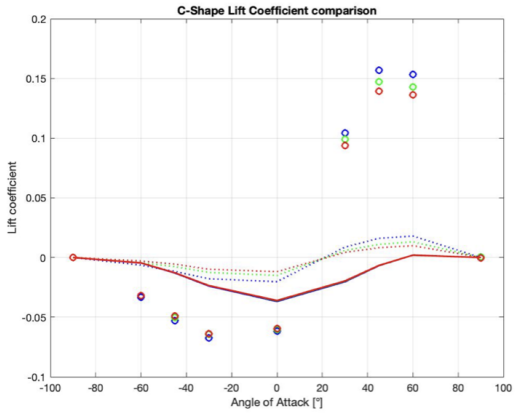

(b) *Lift coefficient*

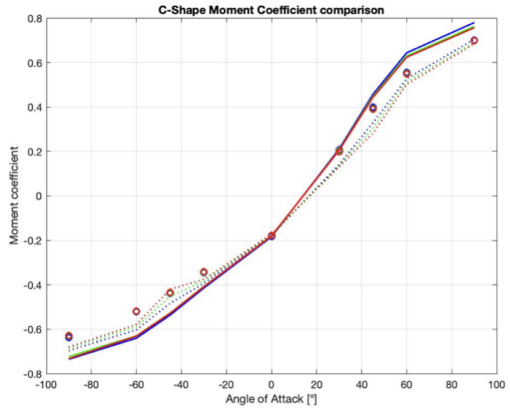

(c) *Moment coefficient*

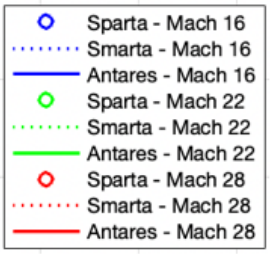

(d) *Legend*

Figure 5.3: C-Shape aerodynamic coefficients results comparison - 100 km.

In tables 5.6, 5.7, the normalized root mean square errors with respect to SPARTA are presented.

NRMSE	Mach 16	Mach 22	Mach 28
C_d	4.84%	4.76%	4.64%
C_l	34.9%	36.3%	37.2%
C_m	2.32%	2.35%	2.88%

Table 5.6: SMARTA Normalized root mean square error - 100 km.

NRMSE	Mach 16	Mach 22	Mach 28
C_d	12.1%	11.1%	5.62%
C_l	38.6%	38.5%	38.4%
C_m	6.06%	5.57%	5.63%

Table 5.7: ANTARES Normalized root mean square error - 100 km.

When the altitude decreases and the free molecular approximation fails, the difference between the codes becomes relevant. SMARTA still gives a good approximation of the drag and moment coefficients, while the estimation of the lift coefficient goes off, especially when the cavity is exposed to the flow. That is due to the fact that the collisions between particles inside the concave surface are not modeled in SMARTA and they become relevant in the transitional regime. However, when looking at the derivatives with respect to the AOA, the SMARTA estimation still provides acceptable results. On the other side, ANTARES gives less accurate results for both the absolute value and the derivatives in relation to the AOA. It is also interesting to see that the effect of the Mach number on the results is low, in any case, the fluctuation is less than 6%.

5.1.3 Case: 80 km Altitude

The simulations at 80 km fall in between the slip flow regime and the transitional regime, as a matter of fact the global Knudsen number in this batch of simulations is:

$$Kn = \frac{\lambda}{l_{ref}} = [0.0975 \div 0.1949]$$

DSMC parameters for the performed runs are shown in table 5.8.

	Simulation Data	Unit
Particles density	3.487e+20	$[1/m^3]$
F_{num}	1.062e+14	-
Δt_{sim}	4.34e-8	[s]
Number of particles	1000000	-

Table 5.8: C-Shape DSMC parameters at 80 km.

In figure 5.4, the comparison between C_d, C_l and C_m of the C-Shape at 80 km altitude is shown.

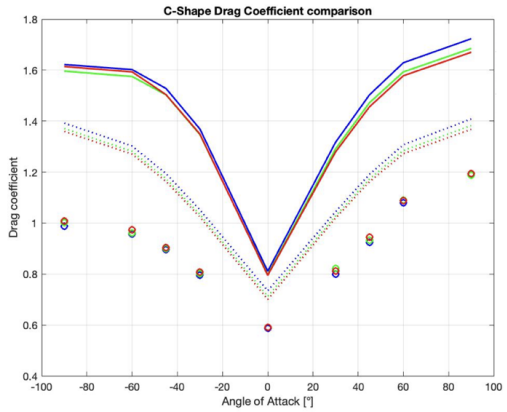

(a) *Drag coefficient*

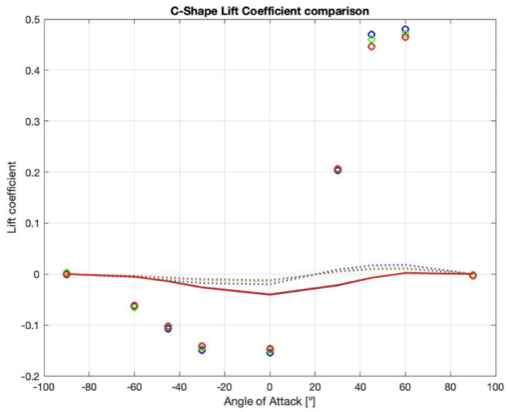

(b) *Lift coefficient*

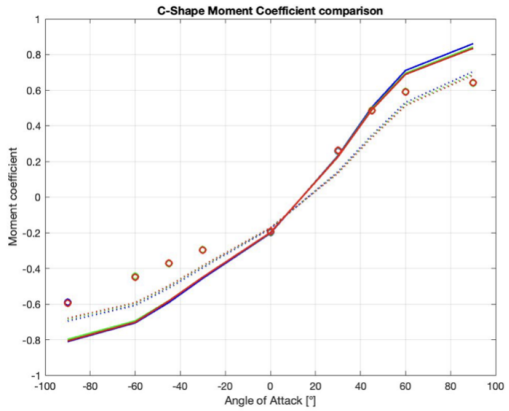

(c) *Moment coefficient*

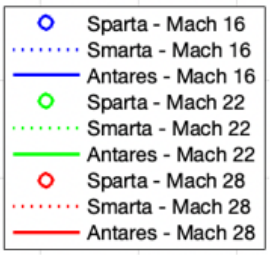

(d) *Legend*

Figure 5.4: C-Shape aerodynamic coefficients results comparison - 80 km.

In tables 5.9, 5.10, the normalized root mean square errors with respect to SPARTA are presented.

NRMSE	Mach 16	Mach 22	Mach 28
C_d	12.4%	12.3%	11.8%
C_l	37.4%	38.1%	38.2%
C_m	6.3%	5.9%	5.6%

Table 5.9: SMARTA Normalized root mean square error - 80 km.

As expected, when the flow becomes more collisional and approaches the continuum regime, SMARTA and ANTARES results lose accuracy with respect to DSMC. In particular, SMARTA still gives a quite reliable approximation of the

NRMSE	Mach 16	Mach 22	Mach 28
C_d	21.3%	20.7%	20.9%
C_l	58.5%	58.7%	58.4%
C_m	13.6%	12.5%	12.3%

Table 5.10: ANTARES Normalized root mean square error - 80 km.

drag and moment coefficient; at the same time, the lift coefficient which has a very low value is far more inaccurate because the effect of the collisions among particles causes high variations of the lift force especially when the particles accumulate inside the cavity exposed to the flow (AOA>0). On the other side, as seen before, ANTARES is quite inaccurate on all the coefficients estimations, while also having a worse approximation of the derivatives with respect to the AOA, especially for the lift coefficient where the latter is not able to evaluate the value inversion when the AOA becomes positive. Based on these considerations, the choice to rule out ANTARES for the aim of the project was made.

After analyzing the results, it can be seen that the great differences between the codes are due to the Knudsen number low value, which in this case, is at the upper limit of the slip flow regime as reported by [24], so it is interesting to examine the temperature and velocity fields around the body to better understand why the software deliver different results.

The plots are obtained using ParaView and show the fields distribution extracted from the DSMC simulations.

Temperature and velocity distribution

In figure 5.5, the translational temperature and the velocity along x axis distributions are shown.

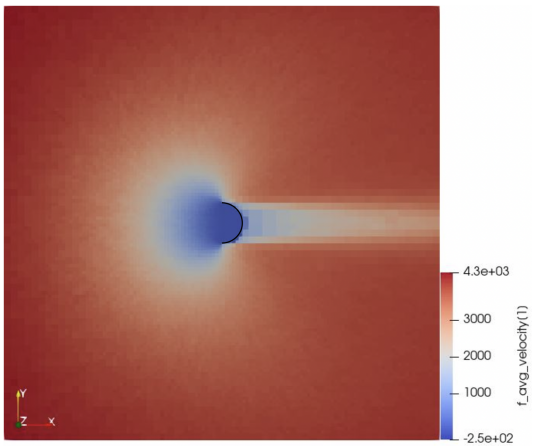

(a) *Velocity distribution along x-axis - 100 km*

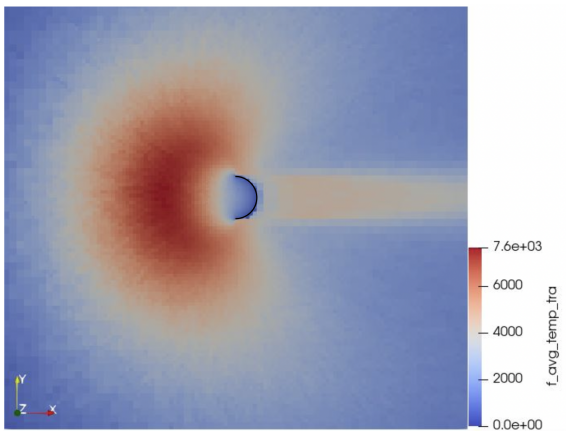

(b) *Translational temperature distribution - 100 km*

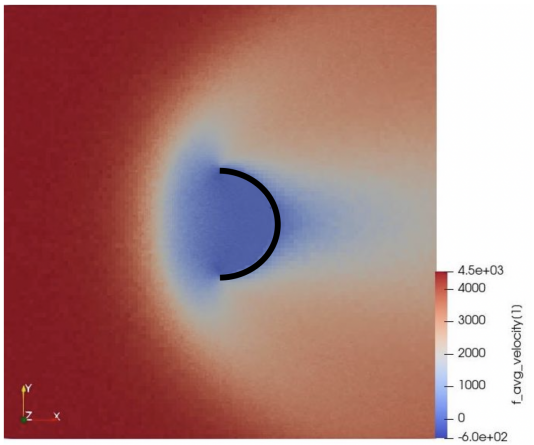

(c) *Velocity distribution along x-axis - 80 km*

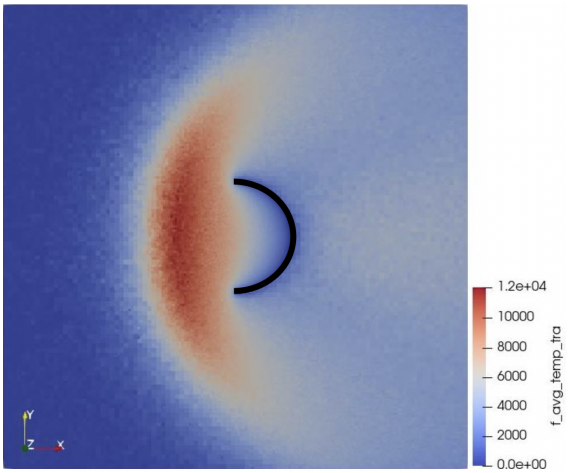

(d) *Translational temperature distribution - 80 km*

Figure 5.5: Macroscopic fields for the C-Shape geometry at 90° AOA - Mach 16 - (a),(b): 100 km altitude. (c),(d): 80 km altitude.

It is possible to see that the translational temperature increases in the area right before the body, while the velocity along the x-axis decreases. That points to the formation of a strong oblique shock wave due to the hypersonic flow and the regime not being free molecular; this phenomenon cannot be modeled in SMARTA and ANTARES that lack the effects of this occurrence in the results, causing lower accuracy in the results with respect to DSMC.

5.2 Flat Plate Results

In this paragraph, the results for the flat plate geometry described in section 4.1.2 are presented.

After the outcome of the C-Shape simulations, ANTARES was discarded since the obtained estimations are considered insufficient. From now on, the analysis and the comparison will be performed only between SMARTA and SPARTA. The runs in this test case are executed for 9 different angles of attack even if the geometry is symmetric to see if the results are coherent in a symmetrical object. The convention used for the AOA is shown in figure 5.6.

AOA	-90°	-60°	-45°	-30°	0°	30°	45°	60°	90°

Table 5.11: AOA considered in the flat plate simulations.

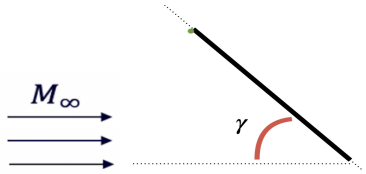

Figure 5.6: Flat plate geometry. The green dot represents the point around which the moment is evaluated.

5.2.1 Case: 140 km Altitude

The analyses at 140 km have been used as a validation to see if the setup and the meshes for both codes are valid, in fact, the flow is in free molecular conditions for all the simulations since the lowest Knudsen number is shown when the AOA is 90° and the exposed surface is maximum:

$$Kn = \frac{\lambda}{l_{ref}} = 212.1$$

The parameters used in the SMARTA simulations are shown in section 4.4, while the SPARTA parameters are shown in table 5.12. It is worth noting that the number of simulated particles is the same as in the 140 km analysis for the C-Shape, to maintain consistency with the statistical error for the DSMC simulations in the free molecular case.

	Simulation Data	Unit
Particles density	8.0152e+16	$[1/m^3]$
F_{num}	1.12e+15	-
Δt_{sim}	5.99e-5	[s]
Number of particles	200000	-

Table 5.12: Flat plate DSMC parameters at 140 km.

In figure 5.7, the aerodynamic coefficients results are represented, while table 5.13 shows the normalized root mean square deviations among the two codes.

Since the regime is free molecular, the estimation of the aerodynamic coefficients provided by SMARTA and SPARTA is extremely similar, with a maximum NRMSE of 0.6% for the lift coefficient at a Mach number of 28. The nature of this error is purely statistical.

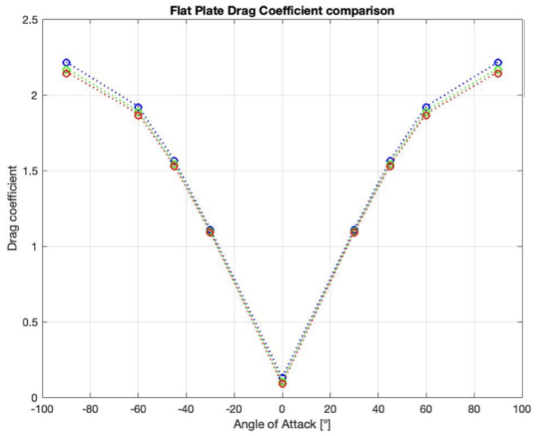

(a) *Drag coefficient*

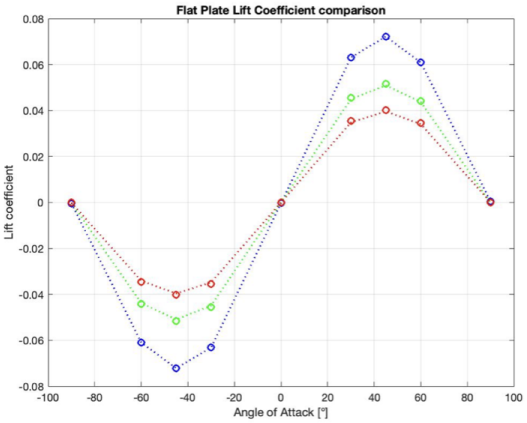

(b) *Lift coefficient*

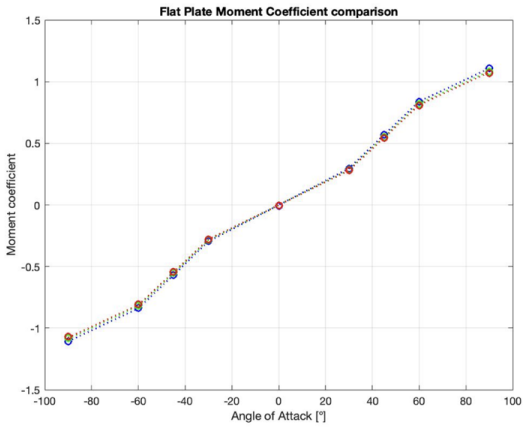

(c) *Moment coefficient*

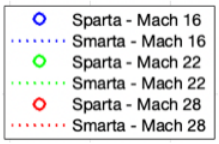

(d) *Legend*

Figure 5.7: Flat plate aerodynamic coefficients results comparison - 140 km.

NRMSE	Mach 16	Mach 22	Mach 28
C_d	0.036%	0.123%	0.237%
C_l	0.046%	0.498%	0.605%
C_m	0.112%	0.152%	0.204%

Table 5.13: SMARTA Normalized root mean square error - 140 km.

5.2.2 Case: 100 km Altitude

The runs carried out at 100 km altitude fall in different aerodynamic regimes, in fact when the flat plate has a 0° AOA with respect to the flow ($l_{ref} = 0.002\ m$), the Knudsen number is:

$$Kn = \frac{\lambda}{l_{ref}} = 76.8$$

This particular case falls in the free molecular flow regime and the solutions given by the two codes agree. However, when the AOA increases, the Knudsen number decreases severely, reaching the lowest value when the maximum surface is exposed ($l_{ref} = 0.1\ m$):

$$Kn = \frac{\lambda}{l_{ref}} = 1.54$$

This case is in the transitional regime and the agreement between the software degrades. DSMC parameters used in this batch of simulations are shown in table 5.14.

	Simulation Data	Unit
Particles density	1.1065e+19	$[1/m^3]$
F_{num}	4.426e+15	-
Δt_{sim}	1.41e-6	[s]
Number of particles	250000	-

Table 5.14: Flat plate DSMC parameters at 100 km.

In figure 5.8, the comparison between C_d, C_l and C_m of the flat plate at 100 km altitude is illustrated.

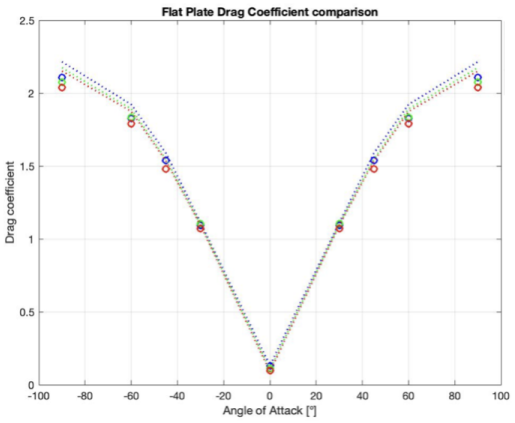

(a) *Drag coefficient*

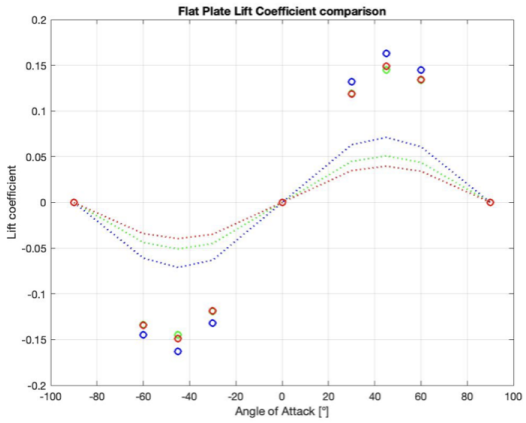

(b) *Lift coefficient*

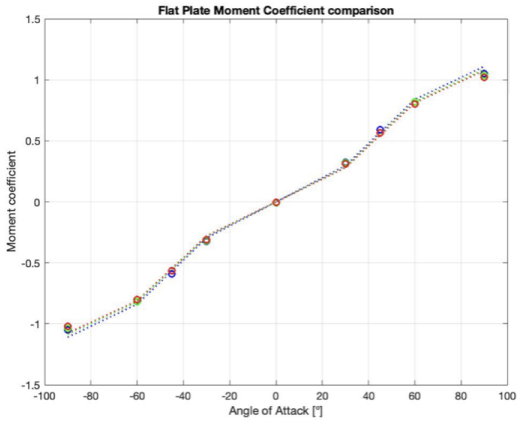

(c) *Moment coefficient*

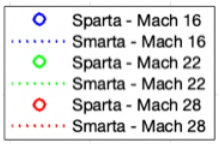

(d) *Legend*

Figure 5.8: Flat plate aerodynamic coefficients results comparison - 100 km.

In table 5.15, the normalized root mean square errors with respect to SPARTA are presented.

NRMSE	Mach 16	Mach 22	Mach 28
C_d	2.15%	2.18%	2.19%
C_l	21.8%	25.8%	28.6%
C_m	1.65%	1.48%	1.66%

Table 5.15: SMARTA Normalized root mean square error - 100 km.

The effect of collisions between particles in the flat plate problem has a lower impact on the accuracy of SMARTA relative to SPARTA since the geometry is simpler and there is no accumulation of particles in a cavity such as in the C-Shape geometry. As expected the approximation provided by the free molecular software is still very good for drag and moment coefficient, while the lift coefficient estimation provides bigger errors because the approximation fails when the surface exposed is maximum and the aerodynamic coefficients approach 0 since the statistical and numerical errors built-in SPARTA have a bigger effect.

5.2.3 Case: 80 km Altitude

To end the flat plate study, simulations at 80 km have been carried out. In this set of simulations the maximum Knudsen number is obtained when the AOA is 0°:

$$Kn = \frac{\lambda}{l_{ref}} = 2.437$$

This case falls in the transitional regime, therefore the comparison between SMARTA and SPARTA should fail, on the other side the most demanding simulations are performed when the Knudsen number is minimum and the AOA is 90°:

$$Kn = \frac{\lambda}{l_{ref}} = 0.048$$

In general, all the simulations are far from the free molecular conditions, consequently, we expect errors in the results comparable to the ones shown for the C-Shape at 80 km altitude. In table 5.16, are shown the DSMC parameters used for the simulations.

	Simulation Data	Unit
Particles density	3.487e+20	$[1/m^3]$
F_{num}	5.521e13	-
Δt_{sim}	4.34e-8	[s]
Number of particles	1600000	-

Table 5.16: Flat plate DSMC parameters at 80 km.

In figure 5.9, are shown the results for the aerodynamic coefficients of the flat plate, while in table 5.17, the normalized root mean square deviations are presented.

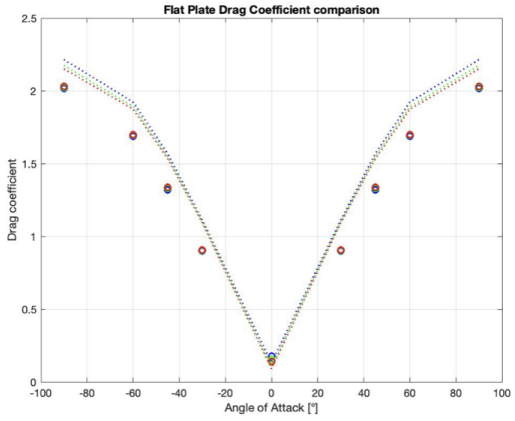

(a) *Drag coefficient*

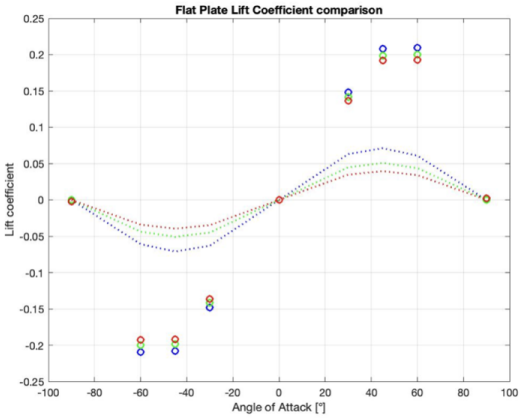

(b) *Lift coefficient*

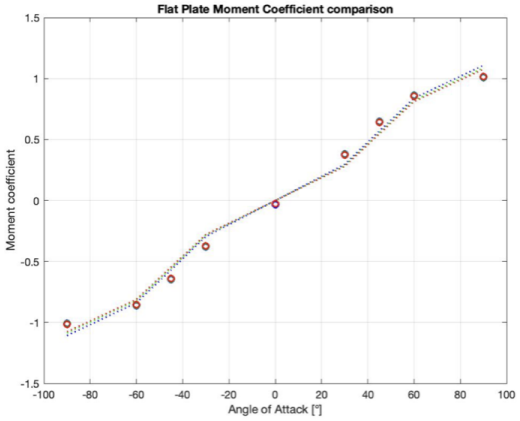

(c) *Moment coefficient*

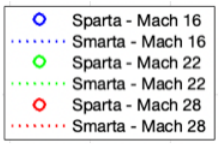

(d) *Legend*

Figure 5.9: Flat plate aerodynamic coefficients results comparison - 80 km.

NRMSE	Mach 16	Mach 22	Mach 28
C_d	5.01%	4.47%	4.18%
C_l	26.2%	29.5%	31.5%
C_m	3.91%	3.78%	3.74%

Table 5.17: SMARTA Normalized root mean square error - 80 km.

The NRMSE extrapolated from this set of simulations provides better values than the C-Shape ones for all the coefficients, moreover, the approximation between SMARTA and SPARTA is still very good even though the flow is in the slip regime for most of the analyses. This is due to the fact that the geometry does not have any critical elements as the cavity where the particles pile up, and the impact of collisions between particles does not affect the comparison between the codes as in the previously analyzed geometry. It is also worth noting that the maximum NRMSE is shown for the lift coefficient as for the C-Shape, and the effect of the Mach number produces a fluctuation of the error lower than 6%, such as in the previous shape.

Temperature and velocity distribution

To end the analyses on the flat plate, in figure 5.10 are reported the temperature and velocity along x-axis distributions at 100 km and 80 km altitude for a Mach number of 16.

Analyzing the temperature and velocity distributions, the existence of a shock wave in front of the flat plate explains why the free molecular estimation made by

SMARTA fails, in fact as pointed out before, the effects of the shock wave due to the collisions between particles when the flow is less rarefied are not modeled in the view factor method used in SMARTA.

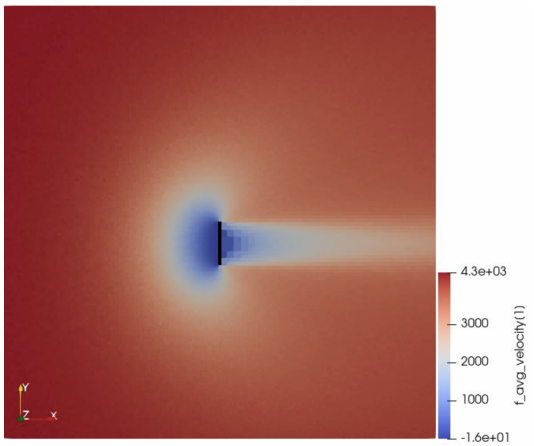

(a) *Velocity distribution along x axis - 100 km*

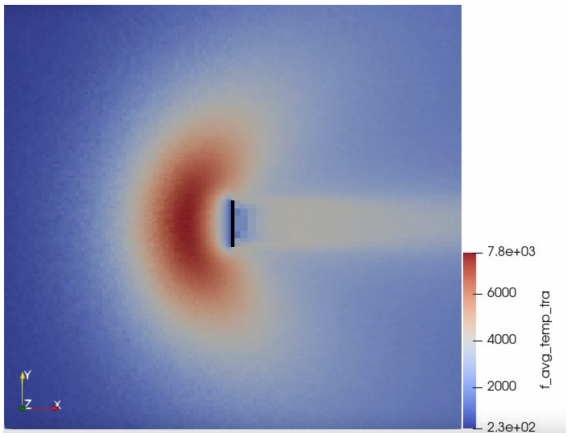

(b) *Translational temperature distribution - 100 km*

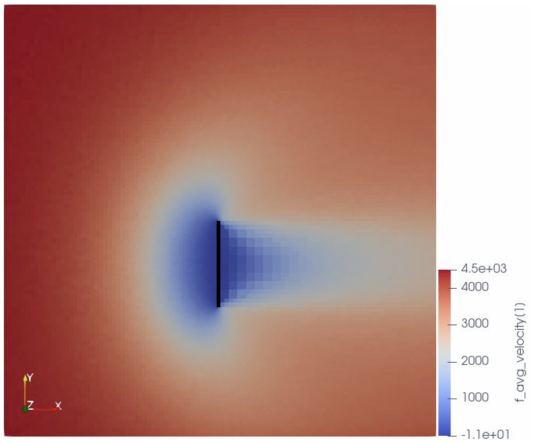

(c) *Velocity distribution along x axis - 80 km*

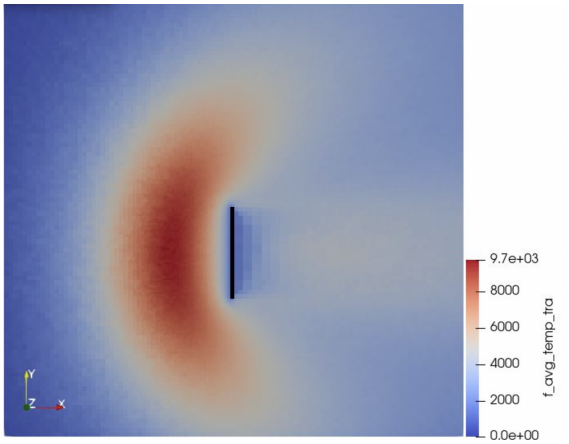

(d) *Translational temperature distribution - 80 km*

Figure 5.10: Macroscopic fields for the flat plate geometry at 90° AOA - Mach 16 - (a),(b): 100 km altitude. (c),(d): 80 km altitude.

5.3 QARMAN Lite Results

In this section, the results for the QARMAN Lite geometry described in section 4.1.3 are presented. This last geometry is considered to compare the effects of the estimations between DSMC and SMARTA on a bigger geometry used in

space applications, where the Knudsen number is lower than the other analyses and the effect of the collisions might be more impacting. The runs are executed for 5 different angles of attack and the convention used for the AOA is shown in figure 5.11.

AOA	0°	45°	90°	135°	180°

Table 5.18: AOA considered in the QARMAN Lite simulations.

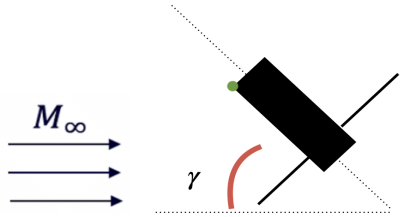

Figure 5.11: QARMAN Lite geometry. The green dot represents the point around which the moment is evaluated.

5.3.1 Case: 140 km Altitude

This set of simulations has again been carried out to validate the surface mesh and see if the correct setup was used for both codes, since the flow is always in free molecular conditions, considering that the Knudsen number is in the following range:

$$Kn = \frac{\lambda}{l_{ref}} = [30.3 \div 62.4]$$

The simulation parameters used for SMARTA are reported in section 4.4, while the DSMC inputs are shown in table 5.19. It is worth noting that again in this case, the number of particles used for the DSMC is the same as the previous free molecular flow test cases, to maintain coherence in the statistical error which is the main error in the free molecular regime.

	Simulation Data	Unit
Particles density	8.0152e+16	$[1/m^3]$
F_{num}	1.12e+15	-
Δt_{sim}	5.99e-5	[s]
Number of particles	200000	-

Table 5.19: QARMAN Lite DSMC parameters at 140 km.

Figure 5.12 shows the results for the C_d, C_l and C_m of QARMAN Lite for this test case.

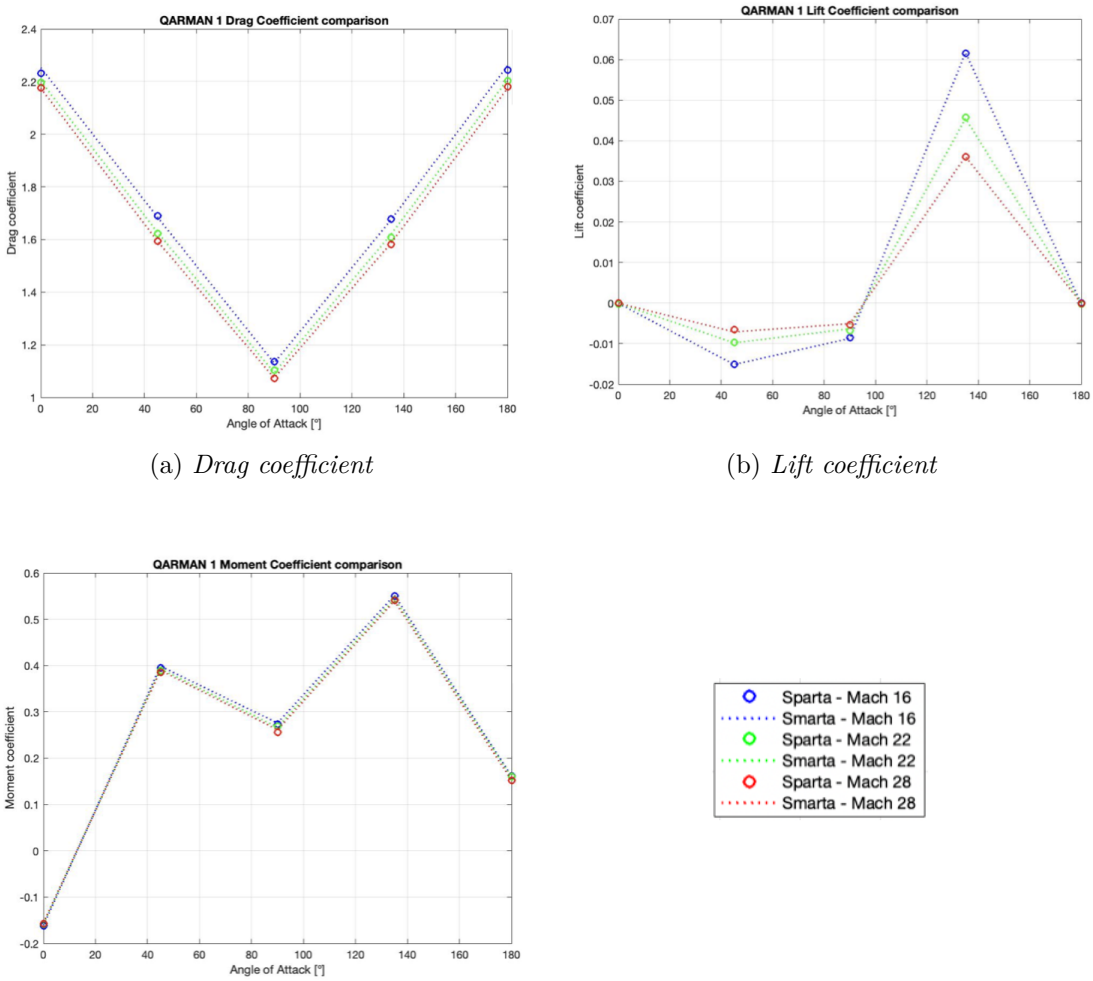

(a) *Drag coefficient*

(b) *Lift coefficient*

(c) *Moment coefficient*

(d) *Legend*

Figure 5.12: QARMAN Lite aerodynamic coefficients results comparison - 140 km.

In table 5.20 it is shown the normalized root mean square error considering DSMC results as a reference.

NRMSE	Mach 16	Mach 22	Mach 28
C_d	0.79%	0.59%	0.35%
C_l	0.22%	0.51%	0.75%
C_m	0.18%	0.33%	0.37%

Table 5.20: SMARTA Normalized root mean square error - 140 km.

As expected, the results indicate great accordance among the two codes in the free molecular regime where the NRMSE is always lower than 1% as a result of the statistical error built-in DSMC due to the number of particles.

5.3.2 Case: 100 km Altitude

The simulations performed at 100 km altitude have a limited Knudsen number range depending on the surface length exposed to the flow:

$$Kn = \frac{\lambda}{l_{ref}} = [0.219 \div 0.452]$$

All the obtained values refer to a transitional flow, where the free molecular hypothesis fails. DSMC parameters used in this batch of simulations are shown in table 5.21.

	Simulation Data	Unit
Particles density	1.1065e+19	$[1/m^3]$
F_{num}	1.450e+14	-
Δt_{sim}	1.41e-6	[s]
Number of particles	615000	-

Table 5.21: QARMAN Lite DSMC parameters at 100 km.

In figure 5.13, the comparison between C_d, C_l and C_m of the considered platform at 100 km altitude is illustrated.

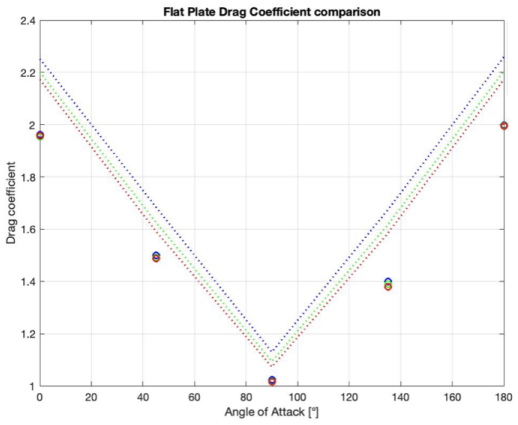

(a) *Drag coefficient*

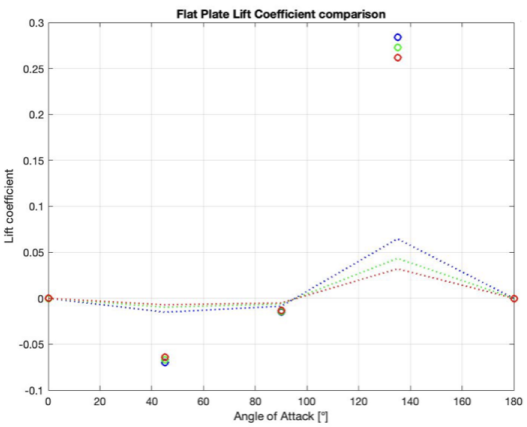

(b) *Lift coefficient*

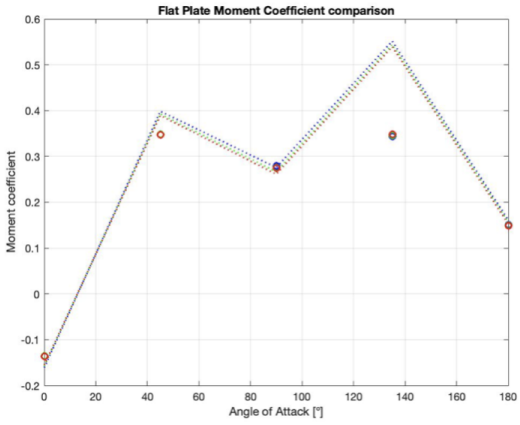

(c) *Moment coefficient*

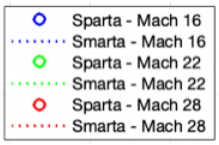

(d) *Legend*

Figure 5.13: QARMAN Lite aerodynamic coefficients results comparison - 100 km.

In table 5.22, the normalized root mean square errors with respect to SPARTA are presented.

NRMSE	Mach 16	Mach 22	Mach 28
C_d	7.92%	7.27%	7.02%
C_l	30.3%	33.1%	34.6%
C_m	19.4%	18.6%	18.1%

Table 5.22: SMARTA Normalized root mean square error - 100 km.

It is easy to notice that the drag and moment coefficient NRMS deviations are higher than the other objects at the same altitude, this is due to the fact that the surface exposed is higher and the Knudsen number is lower than the other shapes. This justifies the larger impact of the collisions, resulting in higher errors even though the number of simulations is lower. At the same time, the lift coefficient has slightly lower errors than in the previous cases, but that is probably due to the fact that when calculating the NRMSE, the impact of the values near 0 on the error is lower than in the other cases. Thus, since the lift coefficient value is close to 0 in 3 out of the 5 simulations, a bigger sample would therefore increase the normalized root mean square errors.

5.3.3 Case: 80 km Altitude

To finalize the presentation of the results, simulations at 80 km altitude for the QARMAN Lite platform have been executed. The Knudsen number in this batch

of runs is the lowest among all the test cases and is in the following range:

$$Kn = \frac{\lambda}{l_{ref}} = [0.00696 \div 0.01433]$$

These values fall in the slip flow region, near the continuum regime. DSMC parameters for this set of simulations are shown in table 5.23.

	Simulation Data	Unit
Particles density	3.487e+20	$[1/m^3]$
F_{num}	1.719e+14	-
Δt_{sim}	4.34e-8	[s]
Number of particles	11000000	-

Table 5.23: QARMAN Lite DSMC parameters at 80 km.

It needs to be said that since the platform dimensions increased significantly with respect to the other objects, the simulations required more memory and time. For example, a single SMARTA simulation for the considered mesh employs around 40 minutes. On the other side, for the DSMC runs, given that the Knudsen number is very small, the number of particles needed to satisfy the DSMC best practices previously expressed is very high, therefore using the simulation model explained in section 4.5, the time needed for each SPARTA simulation is around 10 hours.

In figure 5.14, the comparison between C_d, C_l and C_m of the QARMAN Lite platform at 80 km altitude is shown.

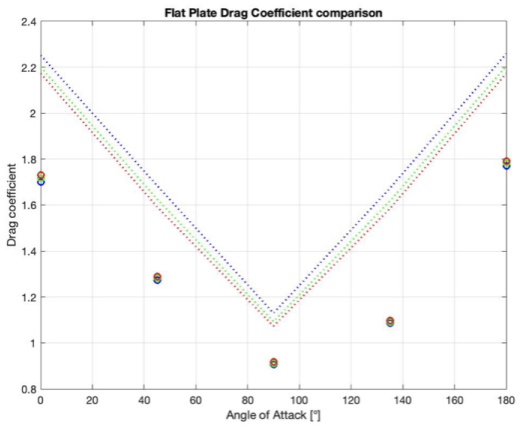

(a) *Drag coefficient*

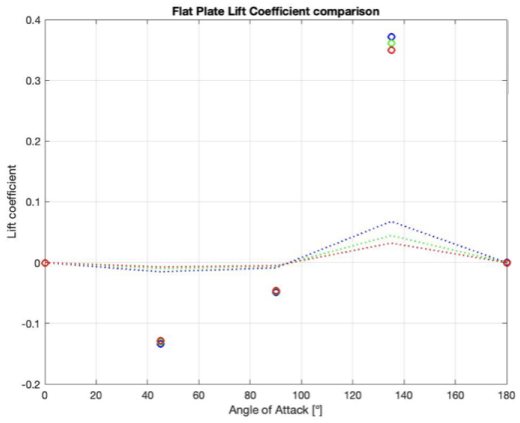

(b) *Lift coefficient*

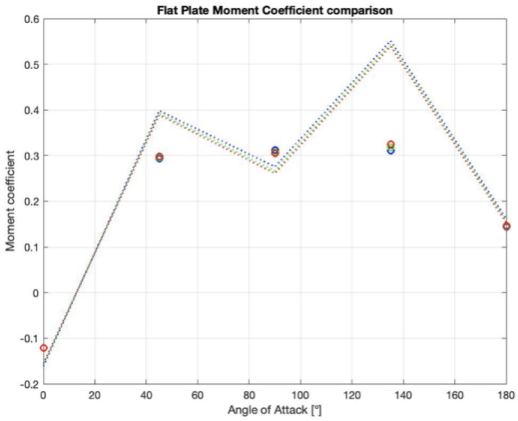

(c) *Moment coefficient*

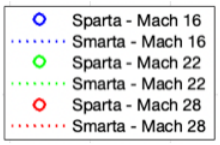

(d) *Legend*

Figure 5.14: QARMAN Lite aerodynamic coefficients results comparison - 80 km.

In table 5.24, are shown the normalized root mean square deviations between SMARTA and DSMC results.

NRMSE	Mach 16	Mach 22	Mach 28
C_d	16.6%	15.6%	14.9%
C_l	31.8%	33.9%	35.1%
C_m	27.2%	25.5%	24.0%

Table 5.24: SMARTA Normalized root mean square error - 80 km.

From the results, it is clear that the estimation among the two software are quite different in absolute value and the differences are evident especially at 135° AOA when the back of the platform is exposed to the flux. In that configuration, the box exposes a small part of itself to the flux and the collisions between particles computed by SPARTA make the free molecular flow approximation fail more than any other configuration. It is also worth noticing that at 0° and 180° AOA the lift coefficient is close to 0 and the two different approaches make the results differ by nearly 1 order of magnitude. Looking at the NRMS deviations table, it is noticeable that the global errors made by SMARTA increase with respect to higher altitudes, especially for the drag and moment coefficient, however, the approximation is still acceptable since the computational cost is strongly decreased.

Temperature and velocity distribution

To complete the analyses, a brief overview of the macroscopic fields around the body is shown.

From figure 5.15, it is possible to see the evolution of the shock wave around the body from the simulations performed at 100 km to the ones executed at 80 km. At 100 km the shock is more diffused, so the velocity and the temperature reach lower values. When the flow is simulated at 80 km, the number of particles and collisions increase, causing the reduction of the shock wave thickness and therefore an increase of the maximum velocity and temperature reached.

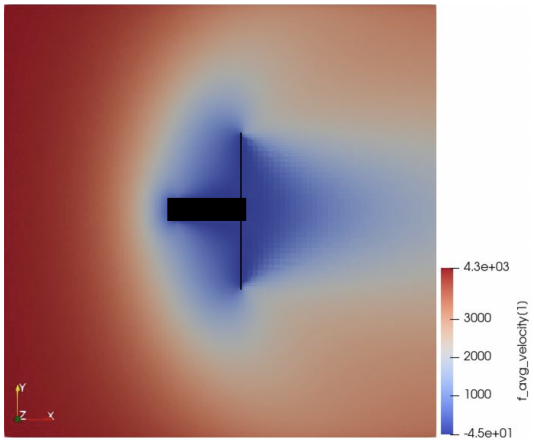

(a) *Velocity distribution along x axis - 100 km*

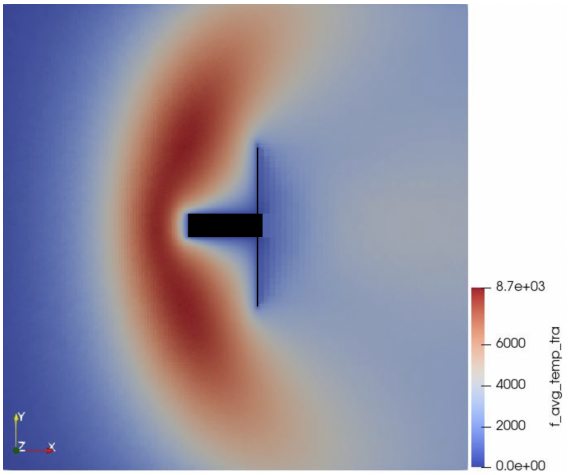

(b) *Translational temperature distribution - 100 km*

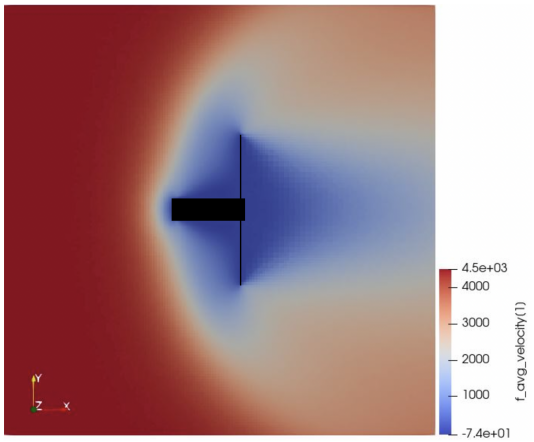

(c) *Velocity distribution along x axis - 80 km*

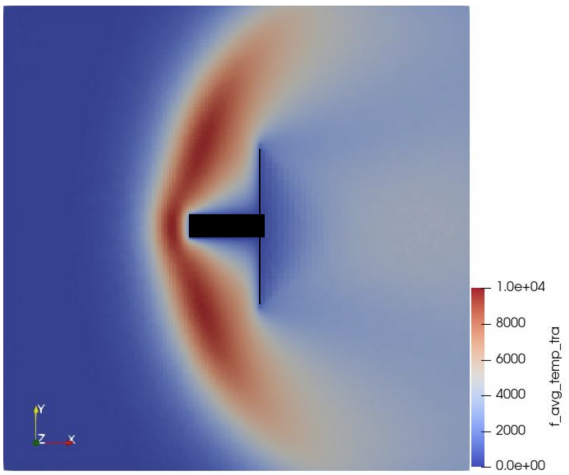

(d) *Translational temperature distribution - 80 km*

Figure 5.15: Macroscopic fields for the QARMAN Lite geometry at 90° AOA - Mach 16 - (a),(b): 100 km altitude. (c),(d): 80 km altitude.

5.4 Reference Point Selection

In this section, the complete path followed to make the object attitude choice for the starting DSMC simulation is shown. After defining the database of the aerodynamic coefficients for the selected shapes on the different codes, the objective is to find a way to select the reference point to perform the initial DSMC simulation and minimize the global error between the DSMC estimations and the approximation obtained from rescaling the SMARTA evaluations starting from the DSMC initial point. Consequently, an initial set of SMARTA simulations will be performed for different AOA to examine how the aerodynamic coefficients evolve with the attitude, and then a SPARTA simulation will be performed at the identified optimum point. To end the process, the approximation of the aerodynamic coefficients with respect to the AOA will be obtained just by scaling the SMARTA results from the single DSMC simulation. This allows us to create a new coefficient for drag (Eq. 5.2), lift (Eq. 5.3), and moment (Eq. 5.4), that represents the outcome of this approach, the extrapolated from SMARTA coefficient defined as:

$$C_{d\alpha,extrapolated} = C_{d_0\,SPARTA} \cdot \left(\frac{C_{d_\alpha}}{C_{d_0}}\right)_{SMARTA} \tag{5.2}$$

$$C_{l\alpha,extrapolated} = C_{l_0\,SPARTA} \cdot \left(\frac{C_{l_\alpha}}{C_{l_0}}\right)_{SMARTA} \tag{5.3}$$

$$C_{m\alpha,extrapolated} = C_{m_0\,SPARTA} \cdot \left(\frac{C_{m_\alpha}}{C_{m_0}}\right)_{SMARTA} \tag{5.4}$$

This coefficient is built by selecting the initial DSMC reference point and then using the SMARTA estimations to evaluate the aerodynamic coefficients with respect to the AOA, from that starting point. In fact, since in DSMCFED there will only be one DSMC simulation, the aim of this section is to see how the error between SPARTA and the extrapolated coefficients evolves when selecting different reference points.

Thanks to this procedure, only one DSMC simulation will be performed allowing a concrete reduction in the computational weight at the cost of a lower accuracy on the results that will be given to the post-processor.

In order to make the selection of the reference point, two different criteria have been identified:

1. **Normalization error**: this parameter has been defined for all the coefficients as shown in equations 5.5, 5.6, 5.7:

$$C_d\ normalization\ error\ [\%] = \left\| \frac{\left(\frac{C_{d_\alpha}}{C_{d_0}}\right)_{SMARTA} - \left(\frac{C_{d_\alpha}}{C_{d_0}}\right)_{SPARTA}}{\left(\frac{C_{d_\alpha}}{C_{d_0}}\right)_{SPARTA}} \right\| \cdot 100 \tag{5.5}$$

$$C_l \text{ normalization error } [\%] = \left\| \frac{\left(\frac{C_{l_\alpha}}{C_{l_0}}\right)_{SMARTA} - \left(\frac{C_{l_\alpha}}{C_{l_0}}\right)_{SPARTA}}{\left(\frac{C_{l_\alpha}}{C_{l_0}}\right)_{SPARTA}} \right\| \cdot 100 \quad (5.6)$$

$$C_m \text{ normalization error } [\%] = \left\| \frac{\left(\frac{C_{m_\alpha}}{C_{m_0}}\right)_{SMARTA} - \left(\frac{C_{m_\alpha}}{C_{m_0}}\right)_{SPARTA}}{\left(\frac{C_{m_\alpha}}{C_{m_0}}\right)_{SPARTA}} \right\| \cdot 100 \quad (5.7)$$

The terms that have 0 as an index, represent the corresponding aerodynamic coefficient value at the selected reference point, while the terms that have α as the index represent the respective aerodynamic coefficient for the considered AOA. That being said, the defined normalization error represents a global relative error between SPARTA and SMARTA, normalized with respect to the SPARTA reference simulation. Thus, the outlined error provides a global view of how the error spreads in the set of simulations. However, this kind of parameter does not show how the error evolves with the attitude.

2. **Sample standard deviation**: this measure is introduced to give another element of comparison between the simulations. It is defined as:

$$s = \sqrt{\frac{\sum_{i=1}^{N}(x_i - \bar{x})^2}{N-1}} \quad (5.8)$$

In the above equation, x is defined for every aerodynamic coefficient as:

$$x_{Cd} = C_{d_{\alpha,SPARTA}} - C_{d\alpha,extrapolated} \quad (5.9)$$

$$x_{Cl} = C_{l_{\alpha,SPARTA}} - C_{l\alpha,extrapolated} \quad (5.10)$$

$$x_{Cm} = C_{m_{\alpha,SPARTA}} - C_{m\alpha,extrapolated} \quad (5.11)$$

N stands for the number of samples, x_i are the observed values of a sample item, while $\hat{x}$ represents the mean value of the observations.

This measure defines the deviation with respect to the mean value between DSMC results and the ones extrapolated using SMARTA simulations, therefore a low value associated with this quantity indicates that the results of the two codes are closer.

If we consider the parameters introduced for the analysis, the aim is to minimize both the standard deviation and the normalization error between DSMC and SMARTA extrapolated results, to obtain better accuracy while making the selection for the reference point to run the SPARTA simulation. A special focus will also be given to the points where the approximation fails mostly to identify possible solutions to this problem. It is important to mention that the selection will be based on considerations from the simulations performed at 100 km and 80 km since the runs carried out at 140 km were only used as a means of validation for the analysis; in fact, their computational cost is significantly lower than the cases where the altitude is lower because the number density of particles is extremely smaller.

5.4.1 C-Shape

In this section, the results relative to the selection of the reference point for the C-Shape geometry are presented.

As pointed out in the previous section, the approximation between SMARTA and SPARTA in a collisional flow fails mostly when the value of the coefficients approaches 0, which is due to the effects of collisions between particles that are not modeled in SMARTA. To start with the selection of the reference point, it is important to choose a point where all the coefficients are not at their minimum absolute value, since the results would be affected by higher errors than in other cases, moreover, it is crucial to identify the coefficient whose maximum absolute value is closer to 0, because the fluctuations caused by the statistical error in DSMC are higher and the effect of collisions is more important.

100 km

To begin with the considerations, it is necessary to analyze the normalization error and the sample standard deviation obtained, to minimize both while selecting different points as a reference. The results for this set of simulations are reported in section 5.1.2. In tables 5.25, 5.26, 5.27, are shown the normalization errors and the sample standard deviations using 3 different reference points at 100 km altitude for different Mach numbers.

	$\|C_d\|$	$\|C_l\|$	$\|C_m\|$	s_{Cd}	s_{Cl}	s_{Cm}
Mach 16	6.65%	144.3%	45.1%	0.024	0.044	0.047
Mach 22	7.01%	144.5%	46.3%	0.027	0.041	0.048
Mach 28	7.23%	130.5%	48.5%	0.027	0.039	0.052

Table 5.25: Normalization error [%] and sample standard deviation using -30° AOA as a reference point for the C-Shape geometry - 100 km

	$\|C_d\|$	$\|C_l\|$	$\|C_m\|$	s_{Cd}	s_{Cl}	s_{Cm}
Mach 16	7.99%	140.7%	45.9%	0.024	0.052	0.040
Mach 22	7.94%	144.1%	45.6%	0.027	0.050	0.035
Mach 28	8.26%	132.2%	47.4%	0.027	0.048	0.039

Table 5.26: Normalization error [%] and sample standard deviation using 0° AOA as a reference point for the C-Shape geometry - 100 km

	$\|C_d\|$	$\|C_l\|$	$\|C_m\|$	s_{Cd}	s_{Cl}	s_{Cm}
Mach 16	11.9%	534.1%	44.1%	0.025	1.284	0.029
Mach 22	13.6%	612.2%	45.4%	0.027	1.415	0.032
Mach 28	13.9%	449.1%	47.5%	0.028	1.047	0.038

Table 5.27: Normalization error [%] and sample standard deviation using 90° AOA as a reference point for the C-Shape geometry - 100 km

The three reference points shown in the tables were selected because they represent 3 focal points in the analysis. The most critical coefficient in this analysis is the lift coefficient since its maximum absolute value is the lowest among the 3 aerodynamic coefficients and the errors between the two codes associated with it are the highest.

The errors relative to the 90° AOA reference point are shown in table 5.27. The shape in this configuration has maximum drag and moment coefficients, while the lift coefficient is close to 0, moreover, the cavity is fully exposed to the flow and the effect of collisions between particles makes the codes produce less similar results, so this configuration is going to be discarded as a possible reference point since the normalization error and the standard deviation for the lift coefficient are not acceptable. The point where the lift coefficient is maximum in absolute value is at 0° AOA, this is the point where the reference should be set since the normalization error produced is at its lowest, however, the drag coefficient is at its minimum absolute value, so a comparison is made with the point where the lift coefficient has its second maximum highest value: -30° AOA. It can be seen that the normalization error is extremely similar for all the coefficients, but the standard deviation for the lift coefficient decreases, while the other standard deviations remain similar, so the obtained results between SPARTA and the SMARTA extrapolation have less discrepancy. Based on these considerations, the selected reference point for this test case is -30° AOA, and the extrapolated coefficients are shown in figure 5.16.

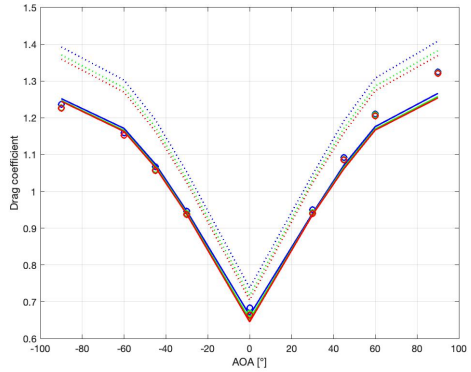

(a) *Drag coefficient - 100 km*

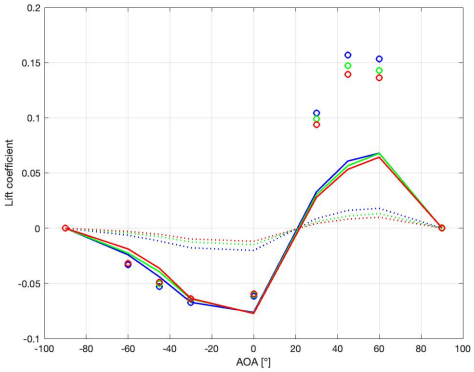

(b) *Lift coefficient - 100 km*

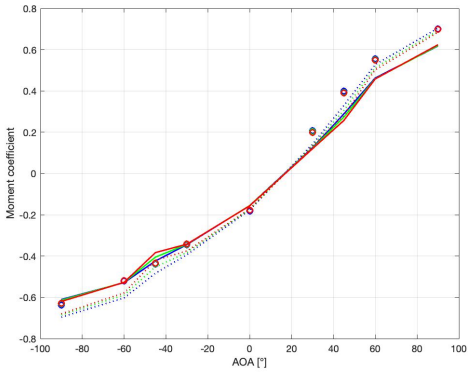

(c) *Moment coefficient - 100 km*

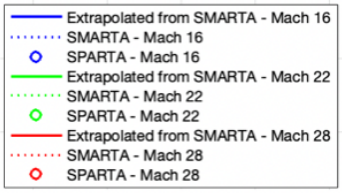

(d) *Legend*

Figure 5.16: Aerodynamic coefficients results when the SPARTA reference point is set at -30° AOA - C-Shape at 100 km altitude.

-90°	1,27%	6,51%	1,56%	6,09%	1,50%	6,49%
-60°	1,02%	2,88%	1,07%	3,34%	0,89%	3,18%
-45°	0,70%	0,81%	0,83%	1,00%	0,74%	1,77%
-30°	0,00%	0,00%	0,00%	0,00%	0,00%	0,00%
0°	2,90%	5,34%	2,63%	6,51%	2,82%	6,37%
30°	2,20%	1,29%	0,61%	2,98%	0,38%	0,70%
45°	1,92%	2,61%	2,02%	2,53%	2,21%	2,81%
60°	2,86%	8,41%	3,13%	8,65%	3,18%	7,60%
90°	4,43%	10,30%	4,88%	9,90%	5,06%	9,58%
	100 km	80 km	100 km	80 km	100 km	80 km
	Mach 16		Mach 22		Mach 28	

0% 10,30%

(a) *Drag coefficient relative errors*

-90°	27,10%	99,60%	33,30%	99,40%	40,50%	98,90%
-60°	27,40%	15,50%	28,70%	21,40%	41,20%	19,21%
-45°	16,70%	4,70%	21,20%	5,50%	25,60%	5,89%
-30°	0,00%	0,00%	0,00%	0,00%	0,00%	0,00%
0°	23,50%	10,30%	27,80%	15,60%	29,50%	16,78%
30°	68,50%	62,90%	69,40%	65,80%	70,20%	67,82%
45°	61,30%	69,40%	61,60%	69,70%	61,80%	69,83%
60°	55,70%	68,20%	52,60%	68,20%	52,70%	68,70%
90°	99,50%	99,30%	96,60%	97,30%	95,18%	91,40%
	100 km	80 km	100 km	80 km	100 km	80 km
	Mach 16		Mach 22		Mach 28	

0% 99,60%

(b) *Lift coefficient relative errors*

-90°	4,24%	12,10%	2,67%	12,28%	1,46%	11,42%
-60°	1,47%	1,10%	1,74%	2,39%	1,86%	2,38%
-45°	3,53%	2,44%	6,99%	2,57%	11,80%	3,74%
-30°	0,00%	0,00%	0,00%	0,00%	0,00%	0,00%
0°	14,80%	33,30%	12,50%	32,60%	11,30%	30,82%
30°	39,90%	58,60%	40,10%	59,78%	39,90%	60,23%
45°	27,70%	46,90%	30,60%	46,99%	34,15%	46,49%
60°	16,80%	32,72%	16,80%	32,90%	16,60%	32,31%
90°	11,80%	17,92%	11,20%	17,75%	10,60%	17,32%
	100 km	80 km	100 km	80 km	100 km	80 km
	Mach 16		Mach 22		Mach 28	
	0%				60,23%	

(c) *Moment coefficient relative errors*

Figure 5.17: Aerodynamic coefficients relative errors when the SPARTA reference point is set at -30° AOA - C-Shape at 100 km and 80 km.

The results obtained from the extrapolation show that the approximation provided by the SMARTA rescaling from the reference point is quite good in terms of drag and moment coefficient, while the lift coefficient which was highlighted as the most critical one shows big discrepancies when the AOA is positive and the cavity is exposed to the flow; in addition, high relative errors between SPARTA and the SMARTA extrapolation are shown when the coefficients are close to 0 as shown in figure 5.17. It is also worth observing that again, the effect of the Mach number on the approximation is less than 10% in all the tested configurations.

80 km

When the altitude decreases and the effect of the collisions among particles becomes more important, errors in the estimation of the aerodynamic coefficients rise as shown in section 5.1.3. That of course reflects in an increase in the standard deviations and the normalization errors obtained following the considered approach. The results for the C-Shape normalization errors and standard deviations at 80 km, for 3 difference reference points are shown in tables 5.28, 5.29, 5.30.

	$\|C_d\|$	$\|C_l\|$	$\|C_m\|$	s_{Cd}	s_{Cl}	s_{Cm}
Mach 16	16.3%	183.3%	91.1%	0.057	0.057	0.112
Mach 22	16.7%	184.1%	91.7%	0.057	0.056	0.112
Mach 28	15.9%	171.9%	90.7%	0.056	0.055	0.110

Table 5.28: Normalization error [%] and sample standard deviation using -30° AOA as a reference point for the C-Shape geometry - 80 km.

	$\|C_d\|$	$\|C_l\|$	$\|C_m\|$	s_{Cd}	s_{Cl}	s_{Cm}
Mach 16	19.3%	187.9%	106.9%	0.057	0.061	0.122
Mach 22	21.3%	191.3%	105.9%	0.058	0.062	0.118
Mach 28	21.9%	181.8%	101.4%	0.057	0.061	0.118

Table 5.29: Normalization error [%] and sample standard deviation using 0° AOA as a reference point for the C-Shape geometry - 80 km.

	$\|C_d\|$	$\|C_l\|$	$\|C_m\|$	s_{Cd}	s_{Cl}	s_{Cm}
Mach 16	32.7%	2854.3%	77.8%	0.059	1.661	0.065
Mach 22	30.6%	2126.2%	79.1%	0.059	1.624	0.066
Mach 28	30.9%	1687.2%	78.9%	0.058	1.561	0.065

Table 5.30: Normalization error [%] and sample standard deviation using 90° AOA as a reference point for the C-Shape geometry - 80 km.

The same reference points as the 100 km altitude case have been examined. As shown previously, selecting a reference point of 90° AOA, where the lift coefficient is roughly 0 creates high absolute errors between the DSMC results and the ones gathered using the scaling approach from SMARTA. Similar considerations as before can be made on the selection of -30° AOA as the reference point for the C-Shape since the normalization errors are comparable with the case where 0° AOA is selected as the reference, while the standard deviations slightly decrease when the reference point is selected where none of the coefficients have their minimum absolute value. Following this study, the reference point for the C-Shape at 80 km is again picked at -30° AOA as in the 100 km case. The comparison among the results for the 3 coefficients is shown in figure 5.18.

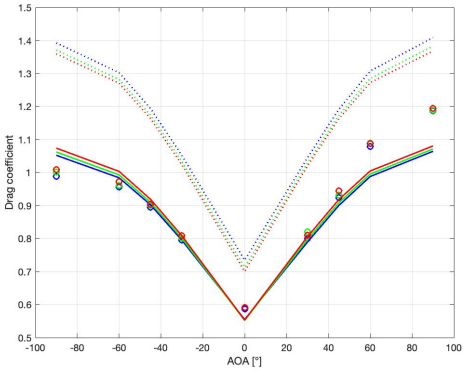

(a) *Drag coefficient - 80 km*

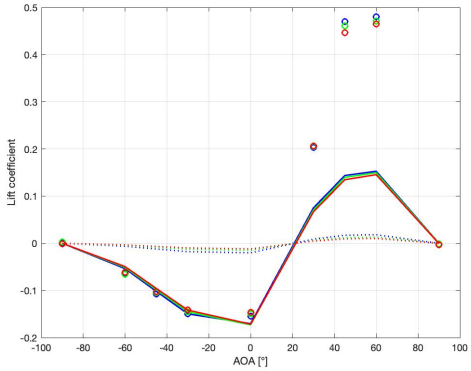

(b) *Lift coefficient - 80 km*

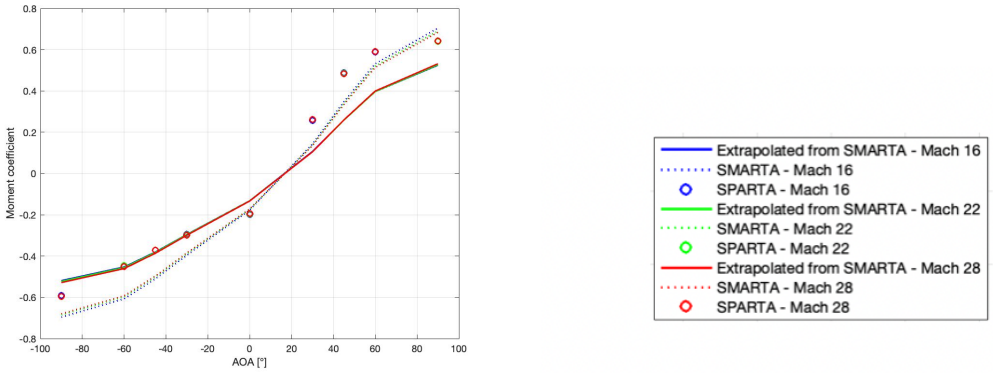

(c) *Moment coefficient - 80 km* (d) *Legend*

Figure 5.18: Aerodynamic coefficients results when the SPARTA reference point is set at -30° AOA - C-Shape at 80 km altitude.

In figure 5.17, it is shown how the relative errors between the SPARTA and the extrapolated from SMARTA solution spread concerning the attitude when the reference point is set at -30° AOA. As pointed out before, the highest errors for the 3 aerodynamic coefficients are focused in the points where the associated coefficient is the lowest in absolute value.

5.4.2 Flat Plate

In this section, the selection of the reference point for the flat plate geometry is explained. The problem will be solved for 100 km and 80 km altitudes where the flow is in the transitional regime, so the estimations made by DSMC and the free molecular flow software have bigger discrepancies. Again, as for the C-Shape geometry, the identified critical coefficient on which the choice will be made is the lift coefficient because it is the one whose maximum absolute value is closer to 0.

100 km

The results on which the considerations will be done are presented in section 5.2.2. In order to make the selection of the reference point for the DSMC simulation, 3 particular AOA were selected as candidates for the final choice. The first analyzed AOA was 90° because the drag and moment coefficient have their maximum value, while the lift coefficient is close to 0. The second candidate is the configuration in which the AOA is 45° because the lift coefficient has its maximum absolute value and the other coefficients are far from their minimum absolute magnitude. The last candidate is 30° AOA where the lift coefficient has the second highest value among all the simulations and the drag and moment coefficients are not near their minimum. The normalization errors and the standard deviations for the selected

reference points between SPARTA and the results extrapolated from SMARTA are shown in tables 5.31, 5.32, 5.33.

	$\|C_d\|$	$\|C_l\|$	$\|C_m\|$	s_{Cd}	s_{Cl}	s_{Cm}
Mach 16	7.46%	145.9%	90.2%	0.033	0.012	0.091
Mach 22	12.5%	149.3%	91.1%	0.045	0.009	0.105
Mach 28	11.9%	166.4%	85.9%	0.030	0.011	0.102

Table 5.31: Normalization error [%] and sample standard deviation using 30° AOA as a reference point for the flat plate geometry - 100 km.

	$\|C_d\|$	$\|C_l\|$	$\|C_m\|$	s_{Cd}	s_{Cl}	s_{Cm}
Mach 16	5.29%	142.5%	88.3%	0.024	0.007	0.056
Mach 22	12.1%	146.4%	87.8%	0.023	0.006	0.038
Mach 28	11.9%	161.9%	83.2%	0.021	0.007	0.052

Table 5.32: Normalization error [%] and sample standard deviation using 45° AOA as a reference point for the flat plate geometry - 100 km.

	$\|C_d\|$	$\|C_l\|$	$\|C_m\|$	s_{Cd}	s_{Cl}	s_{Cm}
Mach 16	7.22%	677.9%	90.5%	0.017	0.147	0.035
Mach 22	12.4%	594.6%	90.5%	0.022	0.079	0.034
Mach 28	14.1%	518.5%	86.6%	0.014	0.093	0.037

Table 5.33: Normalization error [%] and sample standard deviation using 90° AOA as a reference point for the flat plate geometry - 100 km.

The errors shown in table 5.33, show how this candidate is disposable since the percentage errors and the standard deviations for the lift coefficient are inconsistent for all the considered speeds. The other two candidates produce similar results in terms of normalization and standard error since they both have coefficients far from their null value, however, the reference point is selected for this test case at 45° AOA because both the standard and the normalization errors are slightly lower and the absolute value of all the coefficients is higher than the configuration at 30° AOA.

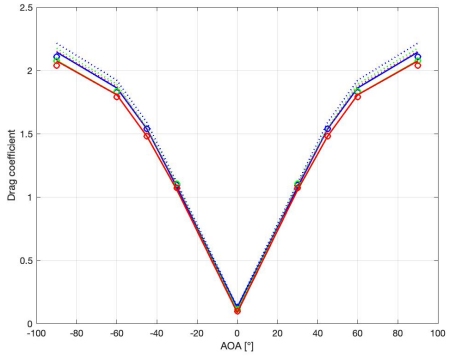

(a) *Drag coefficient - 100 km*

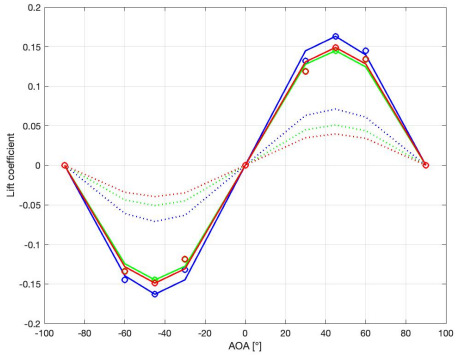

(b) *Lift coefficient - 100 km*

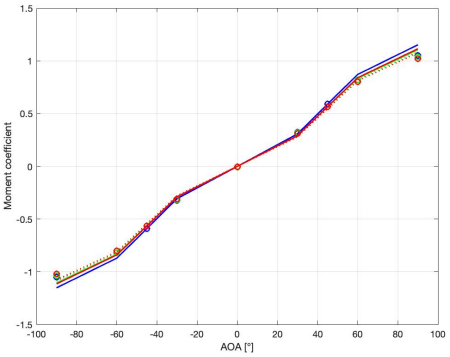

(c) *Moment coefficient - 100 km*

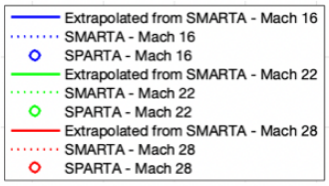

(d) *Legend*

Figure 5.19: Aerodynamic coefficients results when the SPARTA reference point is set at 45° AOA - Flat plate at 100 km altitude.

The results for the coefficients extrapolated from SMARTA starting from the DSMC 45° AOA simulation are shown in figure 5.19. In this case, it is clear that the approximation provided by the extrapolated from SMARTA coefficients is extremely good with respect to SPARTA coefficients especially when their value is far from 0, although the normalized errors are bigger than the C-Shape geometry at the same altitude because the coefficients approach a null value in more configurations, so the errors are concentrated mostly in this points as it is shown in figure 5.20. The errors are shown only for positive AOA since the geometry is symmetrical. At 100 km altitude, considering intermediate AOA (30°,45°,60°), where all the aerodynamic coefficients value is not near 0, the maximum relative error between DSMC and the extrapolated from SMARTA coefficients, is shown for the lift coefficient and it is around 10.5% when the Mach number is maximum, so the approximation provided by the used approach is concretely good in this area; however as highlighted before, it fails when the coefficients approach 0.

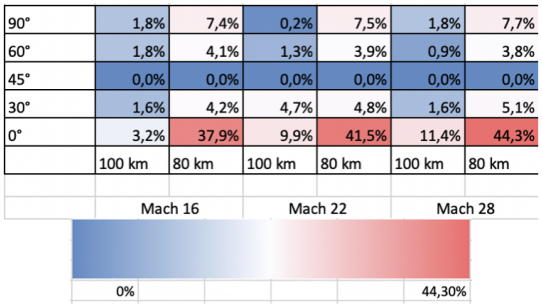

(a) *Drag coefficient relative errors*

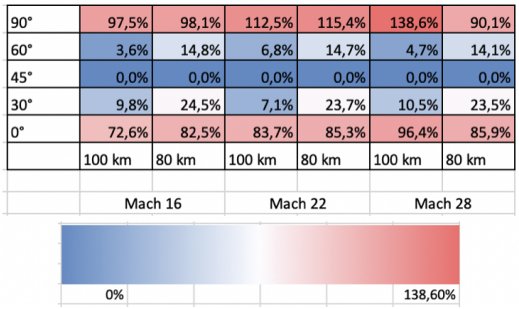

(b) *Lift coefficient relative errors*

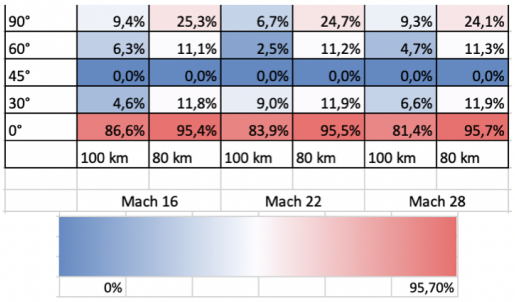

(c) *Moment coefficient relative errors*

Figure 5.20: Aerodynamic coefficients relative errors when the SPARTA reference point is set at 45° AOA - Flat plate at 100 km and 80 km.

80 km

The analyses performed at 80 km altitude provide bigger errors in the estimation of the aerodynamic coefficients, since the influence of the collisions between particles rises and the errors made by SMARTA increase as shown in section 5.2.3. The normalization errors and the standard deviations are shown in tables 5.34, 5.35, 5.36. Similar considerations can be carried out as the 100 km altitude case, in fact using as the reference point 90° AOA for the SMARTA extrapolation, causes high errors in the approximation of the lift coefficient as its value is basically 0 and the estimation between SMARTA and SPARTA is essentially off.

	$\|C_d\|$	$\|C_l\|$	$\|C_m\|$	s_{Cd}	s_{Cl}	s_{Cm}
Mach 16	45.2%	177.1%	119.4%	0.086	0.039	0.244
Mach 22	49.1%	164.7%	119.3%	0.091	0.036	0.243
Mach 28	51.9%	158.3%	119.0%	0.094	0.035	0.241

Table 5.34: Normalization error [%] and sample standard deviation using 30° AOA as a reference point for the flat plate geometry - 80 km.

	$\|C_d\|$	$\|C_l\|$	$\|C_m\|$	s_{Cd}	s_{Cl}	s_{Cm}
Mach 16	40.1%	173.2%	104.5%	0.072	0.024	0.139
Mach 22	43.8%	157.5%	104.3%	0.074	0.022	0.136
Mach 28	46.5%	149.5%	104.1%	0.076	0.021	0.134

Table 5.35: Normalization error [%] and sample standard deviation using 45° AOA as a reference point for the flat plate geometry - 80 km.

	$\|C_d\|$	$\|C_l\|$	$\|C_m\|$	s_{Cd}	s_{Cl}	s_{Cm}
Mach 16	39.3%	1241.8%	110.1%	0.062	0.784	0.100
Mach 22	43.3%	1457.7%	109.7%	0.064	0.891	0.097
Mach 28	46.2%	1458.1%	109.3%	0.066	0.863	0.094

Table 5.36: Normalization error [%] and sample standard deviation using 90° AOA as a reference point for the flat plate geometry - 80 km.

The final choice of the reference point for this configuration is once again between the 30° and 45° AOA cases. Though, as pointed out earlier, the reference point is selected at 45° AOA because the lift coefficient, identified as the critical one, has its maximum value at 45° AOA and that produces the lowest standard and normalization errors between the coefficients extrapolated from SMARTA and the DSMC ones.
The comparison between the evidenced coefficients obtained using 45° AOA as the reference point for the extrapolation, is shown in figure 5.21. The results for the flat plate clearly show lower errors than the C-Shape ones, since the geometry is extremely simpler so the effect of collisions between particles impacts less, producing a better approximation using the free molecule code. The relative errors between the codes are shown in figure 5.20 and as for the 100 km simulations, they are mostly focused on where the coefficients approach a null value.

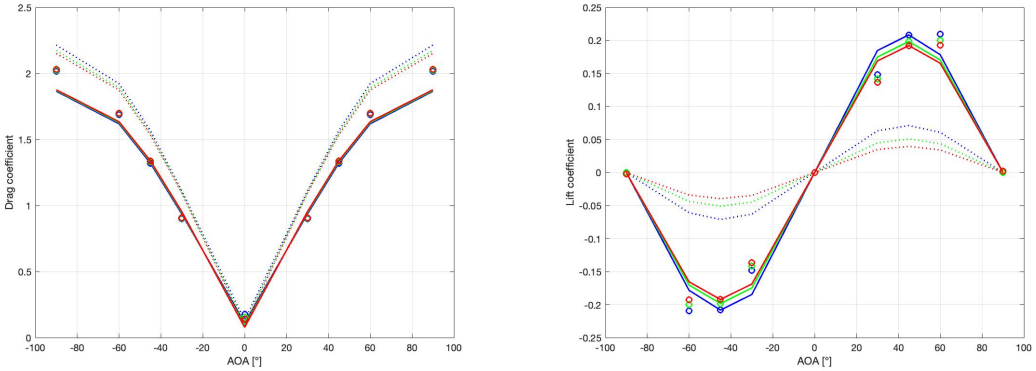

(a) *Drag coefficient - 80 km*

(b) *Lift coefficient - 80 km*

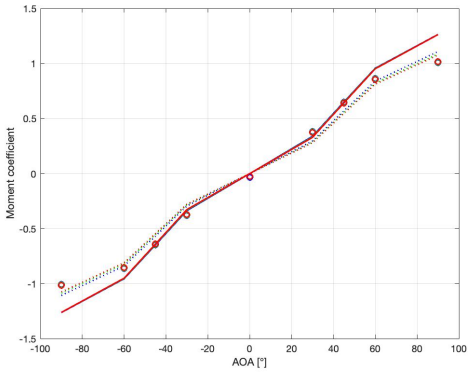

(c) *Moment coefficient - 80 km*

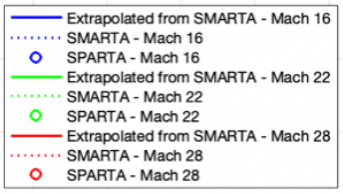

(d) *Legend*

Figure 5.21: Aerodynamic coefficients results when the SPARTA reference point is set at 45° AOA - Flat Plate at 80 km altitude.

5.4.3 QARMAN Lite

In this section, the selection process of the reference point for the QARMAN Lite platform is presented. The study will be performed at 100 km and 80 km altitudes and for all the considered Mach numbers, to validate the procedure used until now to pick the reference point for the initial DSMC simulation. Even here, as in the previous cases, the critical coefficient is the one associated with the lift force since its maximum absolute value is the lowest among the 3 defined coefficients.

100 km

The remarks done in this case are related to the results discussed in section 5.3.2. Again, the objective is to minimize the standard deviation and the normalization errors among the DSMC results and the ones obtained from the SMARTA extrapolation starting from the selected reference point. In tables 5.37, 5.38, 5.39, are shown the standard and normalization errors for 3 different reference points.

	$\|C_d\|$	$\|C_l\|$	$\|C_m\|$	s_{Cd}	s_{Cl}	s_{Cm}
Mach 16	8.79%	237.2%	53.4%	0.042	0.015	0.069
Mach 22	9.71%	256.7%	53.0%	0.045	0.018	0.069
Mach 28	10.5%	285.4%	52.6%	0.048	0.020	0.068

Table 5.37: Normalization error [%] and sample standard deviation using 45° AOA as a reference point for the QARMAN Lite geometry - 100 km.

	$\|C_d\|$	$\|C_l\|$	$\|C_m\|$	s_{Cd}	s_{Cl}	s_{Cm}
Mach 16	12.3%	460.5%	85.5%	0.046	0.084	0.096
Mach 22	12.4%	422.3%	85.6%	0.048	0.085	0.097
Mach 28	13.5%	458.5%	85.9%	0.051	0.086	0.098

Table 5.38: Normalization error [%] and sample standard deviation using 90° AOA as a reference point for the QARMAN Lite geometry - 100 km.

	$\|C_d\|$	$\|C_l\|$	$\|C_m\|$	s_{Cd}	s_{Cl}	s_{Cm}
Mach 16	14.9%	219.2%	80.1%	0.042	0.011	0.062
Mach 22	14.4%	212.3%	79.4%	0.040	0.012	0.061
Mach 28	15.2%	253.6%	80.1%	0.042	0.013	0.061

Table 5.39: Normalization error [%] and sample standard deviation using 135° AOA as a reference point for the QARMAN Lite geometry - 100 km.

The studied reference points represent important configurations for the selected platform. 135° AOA is the point in which the lift coefficient and the moment coefficient are at their maximum value in the analysis, while 90° AOA is the point where drag shows its minimum and lift is close to 0 in SMARTA analysis; then the 45° AOA configuration represents the one in which lift and moment have their second highest absolute value, whereas drag is not at its minimum. 0° and 180° AOA were discarded since the moment and lift coefficients have their lower absolute value and the errors in the approximation between the codes in a collisional flow are higher. Considering the above tables, it is clear that the errors provided by selecting 90° AOA as the reference point are high for both lift and moment coefficient since their value is the lowest one among the 3 selected points. On the other side, the two main candidates to be selected as a reference point show fewer differences among them, however, the 135° AOA configuration minimizes both the standard deviation and the normalization error for the lift coefficient that has been picked as the critical one, given that its value is the closest to 0. Therefore the reference point has been set at 135° AOA for this test case, as it produces the best estimation between the DSMC results and the extrapolation from SMARTA starting from the selected reference point. The results for the extrapolated coefficients are shown in figure 5.22. The relative errors between SPARTA simulations and the coefficients extrapolated from SMARTA at different AOA are shown in figure 5.23. As for the previous analysis, the drag coefficient shows low absolute errors, while the critical points are the ones where the lift coefficient reaches a value close to 0. In fact, the approximation obtained using the explained approach fails mostly at 0°, 90°, and 180° AOA, where the lift and moment coefficients have low absolute values.

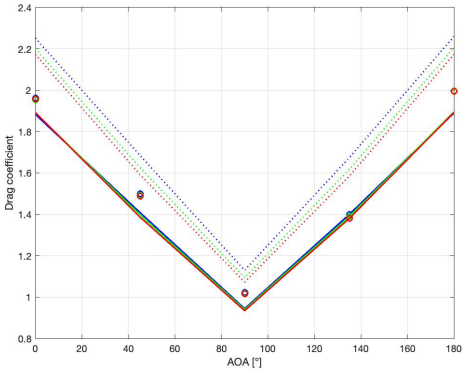

(a) *Drag coefficient - 100 km*

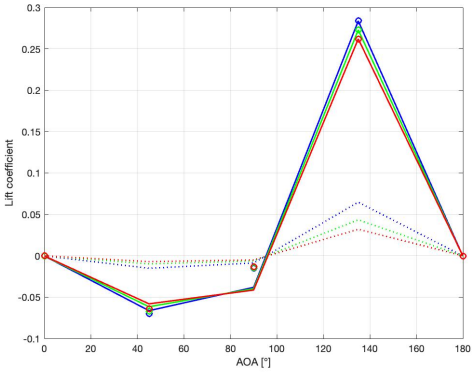

(b) *Lift coefficient - 100 km*

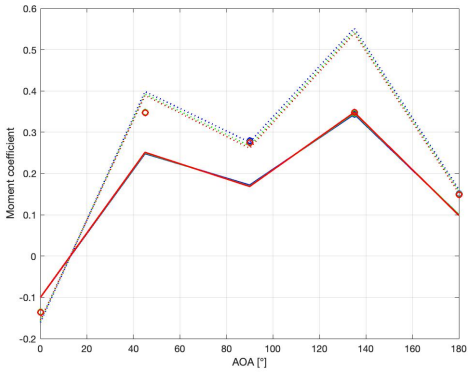

(c) *Moment coefficient - 100 km*

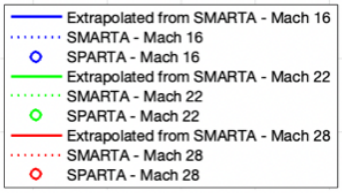

(d) *Legend*

Figure 5.22: Aerodynamic coefficients results when the SPARTA reference point is set at 135° AOA - QARMAN Lite at 100 km altitude.

Subsequently, this continues to prove that the selected approach to estimate the coefficients without performing multiple DSMC simulations, does not work well where the coefficients and the forces are low and the exposed surface to the flow is high because the impact of collisions among particles cannot be caught using the free molecular approximation.

180°	5,4%	17,2%	5,1%	16,6%	5,1%	16,1%
135°	0,0%	0,0%	0,0%	0,0%	0,0%	0,0%
90°	7,8%	19,1%	7,6%	19,1%	8,1%	18,9%
45°	6,0%	14,1%	6,3%	14,6%	6,8%	14,5%
0°	4,0%	14,1%	3,2%	13,6%	3,3%	13,1%
	100 km	80 km	100 km	80 km	100 km	80 km
	Mach 16		Mach 22		Mach 28	

0% 19,10%

(a) *Drag coefficient relative errors*

180°	53,1%	78,4%	53,6%	74,6%	42,7%	80,4%
135°	0,0%	0,0%	0,0%	0,0%	0,0%	0,0%
90°	155,1%	179,1%	179,7%	188,1%	195,2%	219,1%
45°	5,2%	38,2%	7,8%	39,1%	9,2%	39,9%
0°	62,2%	84,5%	69,1%	86,6%	89,1%	99,7%
	100 km	80 km	100 km	80 km	100 km	80 km
	Mach 16		Mach 22		Mach 28	

0% 219,10%

(b) *Lift coefficient relative errors*

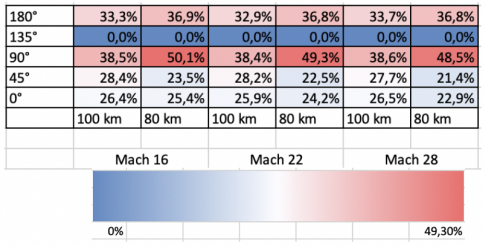

(c) *Moment coefficient relative errors*

Figure 5.23: Aerodynamics coefficients relative errors when the SPARTA reference point is set at 45° AOA - QARMAN Lite at 100 km and 80 km.

80 km

The aerodynamic coefficients results for this test case are explained in section 5.3.3. The study conducted at 80 km altitude directly follows the steps taken at 100 km, in fact, the same reference points were studied and similar considerations can be made. The normalization error and the standard deviations between SPARTA and the extrapolated from SMARTA coefficients, for the selected reference points are shown in tables 5.40, 5.41, 5.42. The errors obtained at 80 km altitude, are of course bigger than the 100 km elevation case, but they follow the same path described before. As a matter of fact, the 90° AOA configuration is again dismissed since the error on the normalization is high for both the lift and moment coefficient.

	$\|C_d\|$	$\|C_l\|$	$\|C_m\|$	s_{Cd}	s_{Cl}	s_{Cm}
Mach 16	17.7%	398.5%	49.7%	0.098	0.106	0.073
Mach 22	18.1%	373.1%	48.8%	0.096	0.109	0.071
Mach 28	17.9%	321.1%	48.1%	0.094	0.111	0.069

Table 5.40: Normalization error [%] and sample standard deviation using 45° AOA as a reference point for the QARMAN Lite geometry - 80 km.

	$\|C_d\|$	$\|C_l\|$	$\|C_m\|$	s_{Cd}	s_{Cl}	s_{Cm}
Mach 16	25.2%	627.1%	127.1%	0.098	0.022	0.148
Mach 22	25.3%	612.9%	123.9%	0.097	0.031	0.147
Mach 28	25.3%	578.3%	120.3%	0.096	0.043	0.145

Table 5.41: Normalization error [%] and sample standard deviation using 90° AOA as a reference point for the QARMAN Lite geometry - 80 km.

It is worth noting that in the 90° AOA configuration the standard deviation on the lift coefficient is unexpectedly lower than in the 45° AOA case, where the normalization error is lower. Following these considerations, once again the reference

	$\|C_d\|$	$\|C_l\|$	$\|C_m\|$	s_{Cd}	s_{Cl}	s_{Cm}
Mach 16	32.5%	306.4%	71.2%	0.114	0.023	0.072
Mach 22	32.2%	324.5%	69.8%	0.111	0.023	0.069
Mach 28	31.6%	361.4%	68.4%	0.107	0.024	0.067

Table 5.42: Normalization error [%] and sample standard deviation using 135° AOA as a reference point for the QARMAN Lite geometry - 80 km.

point has been set at 135° AOA since the standard deviation and the normalization error on the lift coefficient are minimum. The results derived from this choice are shown in figure 5.24, while the relative errors between the DSMC solutions and the coefficients extrapolated from SMARTA starting from the selected reference point are displayed in figure 5.23.

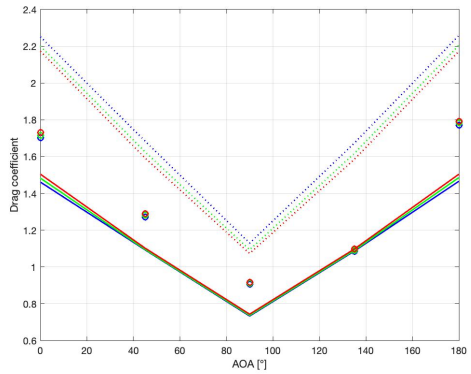

(a) *Drag coefficient - 80 km*

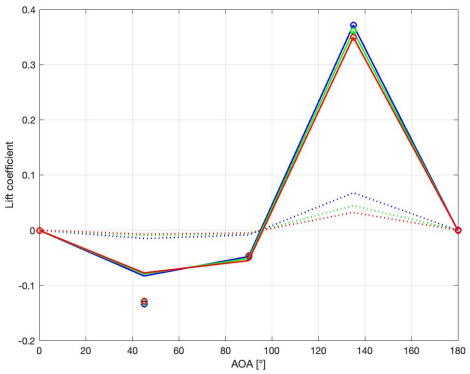

(b) *Lift coefficient - 80 km*

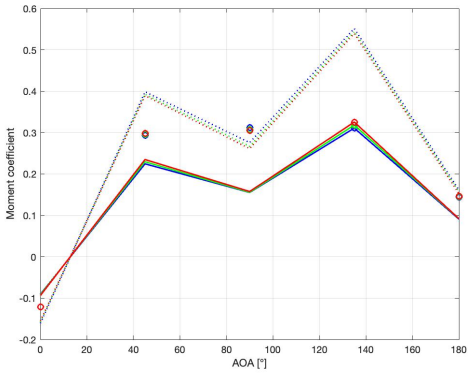

(c) *Moment coefficient - 80 km*

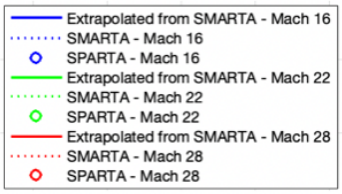

(d) *Legend*

Figure 5.24: Aerodynamic coefficients results when the SPARTA reference point is set at 45° AOA - QARMAN Lite at 80 km altitude.

The same observations as the 100 km case can be carried out. The drag coefficient errors are still contained below 20% for all the simulations, while the estimation of the moment coefficient provides maximum relative errors around 50% at 90° AOA. As in the other cases, the maximum errors are found for the lift coefficient especially when its value is close to 0, where the errors obtained among the codes always increase because the collisionless approach fails. In this shape the errors are augmented since the surface exposed to the flow is larger than the other shapes.

5.4.4 Results Summary

In this section, the obtained results are summarized with the aim of creating a general procedure that helps selecting the reference point to perform the starting DSMC simulation from which the aerodynamic coefficients will be rescaled using the estimation provided by SMARTA. This procedure, as explained before, is intended to minimize the errors between the DSMC simulations outcome and the results obtained using the SMARTA coefficients extrapolation from the selected reference point.

Following the considerations made until this point, it is clear that the estimation using the studied approach fails when the coefficients are close to a null value and the exposed surface to the flow is high since the free molecular approximation misses the effect of the collisions between particles treated by DSMC. Therefore it is important to identify which coefficient has the lowest maximum absolute value among all, it will be considered as the critical one and the selection will be made taking into account its evolution with respect to the AOA.

Since only one DSMC simulation will be performed, a set of SMARTA simulations will be conducted to extrapolate the trend of all the needed coefficients against the angle of incidence; after that, the critical coefficient (as defined before) will be extracted and a first tentative reference point will be selected where the given coefficient has its maximum absolute value, so when the error in the selection should be minimum, as evidenced in the previous section.

After selecting the first candidate point, a loop is needed to see that all the other aerodynamic coefficients are not at their minimum in absolute value, since that would increase the errors in their estimation. In the case that one of the coefficients has its minimum absolute value in the selected reference point, the latter will be changed to the point where the critical coefficient has its second absolute maximum value. The loop ends when the coefficients at the selected reference point comply with the condition imposed, thereby all the coefficients could be estimated ensuring that none of them has extremely high errors. At this point, the attitude of the object with respect to the flow is set and the DSMC simulation can be performed at the given conditions.

To conclude the procedure, the extrapolated coefficients will be produced using the approach explained in section 5.4 and the final results in terms of aerodynamic

coefficients will be passed on to the trajectory module that will use them for the propagation of the trajectory in the software. A flow chart for the described procedure is shown in figure 5.25.

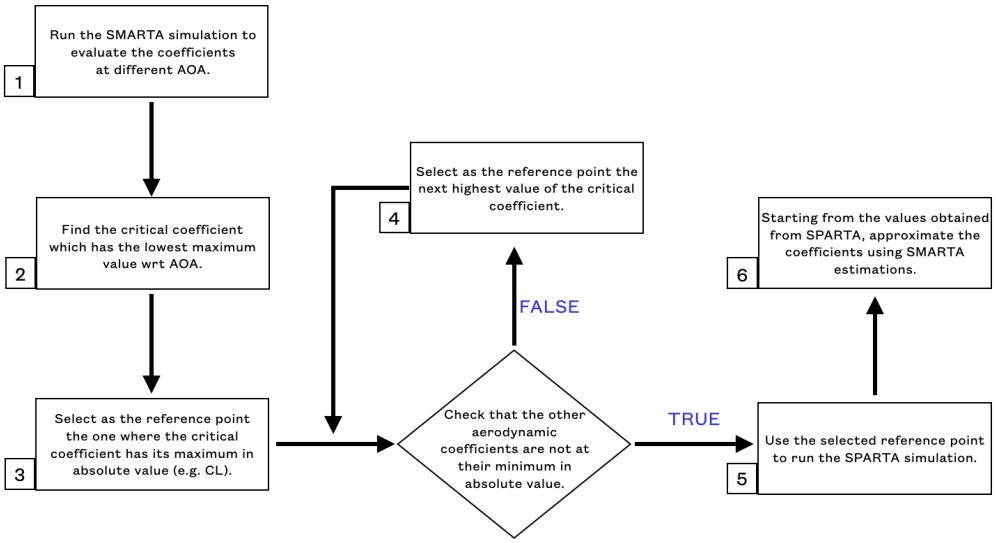

Figure 5.25: Final proposed strategy for the DSMC reference point selection.

5.5 Concluding Remarks

In this chapter, the estimation of the aerodynamic coefficients using 3 different software is shown. It has been demonstrated that the Newtonian solver (ANTARES) is insufficient in terms of performance due to the strong simplifications adopted by the method. On the other side, the comparison between DSMC and SMARTA is very accurate in the limit of a free molecular flow at 140 km altitude, while it still gives an acceptable approximation at lower altitudes where the effect of collisions between particles increases and the flow is in the transitional regime.

Based on these results, a simplified approach has been pursued, to use SMARTA to complement DSMC results and reduce the computational cost of the analyses to estimate the aerodynamic coefficients. As a matter of fact, it has been shown that by selecting a particular attitude to perform one DSMC simulation on an object, it is possible to reduce the errors between the DSMC estimation and the one provided by shifting from the selected reference point, the aerodynamic coefficients evaluated with SMARTA. This approach has shown good results where the value of the coefficients is not approaching 0, while the relative errors increase when the studied configuration features coefficients with close to a null value. Moreover, this procedure has been tested for different Mach numbers to cover all the re-entry possibilities, and the relative errors between the estimated aerodynamic coefficients do not differ by more than 10% for all the speed configurations analyzed.

Chapter 6

Conclusions

The aim of this thesis was to perform computations of the aerodynamic coefficients of different objects during the re-entry to find ways to reduce the computational cost of the analyses. The work has been carried out at the von Karman Institute for Fluid Dynamics in the context of the DSMCFED project. At the basis of the project is the need to develop a toolset to evaluate the aerothermodynamics and the thermo-structural behavior of spacecraft during the re-entry, thanks to the interaction between 3 codes: a trajectory propagator, a thermo-structural code, and a flow code.

The work explained in this thesis complements the development of the flow code based on SPARTA, which is a DSMC code. The DSMC code is selected since analyses in the free molecular and transitional regimes are performed and the latter method has been selected as it is the most efficient in these conditions. However, the computational cost of DSMC analysis drastically increases when the flow approaches the continuum regime at lower altitudes since the number of collisions among the simulated particles rises, so different approaches are sought.

The idea behind the work is to perform a starting DSMC simulation to identify the aerodynamic coefficients of the objects at a fixed attitude, and then use lower fidelity codes to estimate the value of the coefficients at different attitudes from the starting point previously identified. Two codes developed at VKI were identified as possible candidates to pursue this approach: ANTARES and SMARTA. ANTARES is a Newtonian flow solver, while SMARTA is based on the view-factor method and has been validated in the free molecular regime. The DSMC analyses have been performed in 2D as a simplification to reduce the computational cost of the simulations.

The analyses have been carried out at 3 different altitudes: 140 km, 100 km, and 80 km. These altitudes were selected to analyze how the effects of the flow regime and collisions among particles affect the errors in the estimation of the aerodynamic coefficients with respect to DSMC. Moreover different Mach number configurations have been studied to see how the flow speed impacts the estimation

over the re-entry trajectory.

Three different shapes have been taken into account to see how different geometries behave in the different flow regimes and how the particles accumulation in concave surfaces makes the estimation differ.

The preliminary analyses on the first shape have shown that SMARTA might be a good candidate in the estimation of the aerodynamic coefficients, while ANTARES accuracy is extremely lower, so it has been discarded as a possible option; the subsequent analyses have been performed by comparing SPARTA and SMARTA results.

In the free molecular regime (140 km) the outcome of the 2 codes is extremely good, showing a maximum normalized root mean square deviation for all the aerodynamic coefficients in the different shapes, lower than 1%. When the flow regime becomes transitional the two software start to produce different results because the free molecular approximation fails and the effect of collisions between particles impacts the outcome. At 100 km and 80 km, the flow is in the transitional regime and the normalized root mean square deviation between the SPARTA and SMARTA analyses increases, in particular, the drag and moment coefficients show a maximum NRMSE of 27%; on the other side, the lift coefficient provides lower accuracy. The main reason behind the lower accuracy is the fact that the free molecular approximation in SMARTA is not applicable, moreover, the statistical error built-in DSMC amplifies these errors since the absolute value of the lift coefficient is low. It has also been noticed that the Mach number does not affect the estimation as the altitude does, in fact, the fluctuation of the NRMSE with respect to the Mach number at a fixed altitude is lower than 8%.

The final step of the work has been based on trying to find a way to select the object attitude for the starting DSMC simulation in order to reduce the error between the complemented DSMC results obtained through SMARTA and the actual DSMC outcome. To perform the selection, two different errors were defined: the normalization error and the standard deviation between the two aforementioned datasets. It has been shown that the lift coefficient should be used as the sizing coefficient to select the reference configuration since it is the smallest in absolute value among the 3 coefficients and the errors produced between the two codes increase as the coefficients approach the null value. The best way to reduce the defined errors has been identified in selecting a reference point for the DSMC simulation where the lift coefficient has its maximum absolute value because the approximation of the derivatives of the coefficients with respect to the AOA between the two codes is more consistent.

Finally, a strategy to be implemented in the DSMCFED toolset has been preliminarily proposed, to complement the unique DSMC simulation using SMARTA and estimate the aerodynamic coefficients of the objects at different attitudes while minimizing the absolute errors with respect to DSMC simulations.

Possible Future Work

The discussed work has the purpose to provide a preliminary approach to solve the problem related to the high computational cost of multiple DSMC simulations for calculating the aerodynamic coefficients of objects during re-entry.

Starting from this work, it is necessary to extend the DSMC analyses to a 3D environment to see how the other aerodynamic coefficients are affected using this approach, since using 2D simulations only 3 coefficients are analyzed. Moreover, the models of the simulations could be extended to include surface and particles reaction to see how these elements affect the characterization.

To conclude, it is worth recalling that the outcome of the flow code is the input of the trajectory propagator in the DSMCFED toolset. Then, if the proposed strategy leads to a rise of the errors when extended to more coefficients and no further approaches are found, a possible idea could be to optimize the complementation of DSMC results with SMARTA, performing a study on which coefficients affect mostly the re-entry trajectory in order to reduce the estimation error on the aerodynamic coefficients that have more impact on the trajectory propagation.

Bibliography

[1] NRLMSIS Atmosphere Model. https://kauai.ccmc.gsfc.nasa.gov/instantrun/msis.

[2] SMARTA. https://gitlab.com/pietroparodi/smarta/.

[3] SPARTA Direct Simulation Monte Carlo Simulator. http://sparta.sandia.gov/.

[4] Speed Regimes, Hypersonic Re-Entry. https://www.grc.nasa.gov/WWW/BGH/hihyper.html.

[5] Tecplot user manual. https://www.tecplot.com/documentation/.

[6] John D. Anderson. *Hypersonic Flow Theory*. Academic Press INC, 1959.

[7] Samuel J. Araki. Radiosity view factor model for sources with general distribution. *Journal of Computational Physics*, 406:109146, 2020.

[8] Federico Bariselli, Stefano Boccelli, and Aldo Frezzotti. A hands-on introduction to the direct simulation monte carlo method. unpublished presentation, April/May 2022.

[9] Paritosh Bide. *DSMC simulations of near-continuum hypersonic flows: code acceleration techniques and comparisons with state-of-the-art CFD solutions*. PhD thesis, 10 2021.

[10] G.A. Bird. *Molecular Gas Dynamics and the Direct Simulation of Gas Flows*. Number v. 1 in Molecular Gas Dynamics and the Direct Simulation of Gas Flows. Clarendon Press, 1994.

[11] G.A. Bird. *The DSMC Method*. CreateSpace Independent Publishing Platform, 2013.

[12] Iain D. Boyd and Thomas E. Schwartzentruber. *Nonequilibrium Gas Dynamics and Molecular Simulation*. Cambridge Aerospace Series. Cambridge University Press, 2017.

[13] Valerio Carandente, Michele Iacovazzo, and Chiara Boffa. Aerothermal analysis of a sample-return reentry capsule. *Fluid Dynamics and Materials Processing*, 9:461–484, 12 2013.

[14] Tianfeng Chai and Roland R Draxler. Root mean square error (rmse) or mean absolute error (mae). *Geoscientific Model Development Discussions*, 7(1):1525–1534, 2014.

[15] Paul A. Chambre and Samuel A. Schaaf. *Flow of Rarefied Gases*. Princeton

Legacy Library, 2017.

[16] Chan-Hong Chung, Suk C. Kim, Robert M. Stubbs, and Kenneth J. De Witt. Low-density nozzle flow by the direct simulation monte carlo and continuum methods. *Journal of Propulsion and Power*, 11(1):64–70, 1995.

[17] Nishanth Dongari, Ashutosh Sharma IITK, and F. Durst. Pressure-driven diffusive gas flows in micro-channels: From the knudsen to the continuum regimes. *Microfluidics and Nanofluidics*, 6:679–692, 05 2009.

[18] Thomas Durbin, Guillaume Grossir, and Olivier Chazot. Hypersonic aerodynamic predictions for arbitrary geometries using antares. 09 2022.

[19] Paulo Flores. *Euler Angles, Bryant Angles and Euler Parameters*, volume 168. 03 2015.

[20] V.S Galkin and V.A Zharov. Exact solutions of the boltzmann—maxwell kinetic equation. *Journal of Applied Mathematics and Mechanics*, 68(1):1–23, 2004.

[21] Christophe Geuzaine and Remacle Jean-Francois. Gmsh: a three-dimensional finite element mesh generator with built-in pre- and post-processing facilities. *International Journal for Numerical Methods in Engineering*, 79(11):1309–1331, 2009.

[22] Mitalas G.P. and Stephenson D.G. Fortran iv programs to calculate radiant energy interchange factors. *Technical report, National Research Council of Canada*, 1966.

[23] Wallace D. Hayes and Ronald F. Probstein. *Hypersonic and High-Temperature Gas Dynamics, Third Edition*. American Institute of Aeronautics and Astronautics, Inc., Reston, Virginia, 2019.

[24] Satish Kandlikar and William Grande. Evolution of microchannel flow passages–thermohydraulic performance and fabrication technology. *Heat Transfer Engineering*, page 5, 01 2003.

[25] Keith Christopher Kannenberg. *Computational methods for the Direct Simulation Monte Carlo Technique with application to plume impingement*. PhD thesis, May 1998.

[26] Candice I. Kaplan and Ian D. Boyd. Drag analysis of a tumbling 3u cubesat experiencing orbital decay. *AIAA Paper 2109-3264*, June 2019.

[27] Earle H. Kennard. *Kinetic theory of gases*. McGraw-Hill Book Company, INC., 1938.

[28] D. Kleppner and R.J. Kolenkow. *An Introduction to Mechanics*. Cambridge University Press, 2010.

[29] Angelos Klothakis, Georgios Lygidakis, and Ioannis Nikolos. Numerical analysis of rarefied gas flows using the academic cfd code galatea. 06 2016.

[30] Lester Lees. Hypersonic flow. *Fifth International Aeronautical Conference, Los Angeles*, pages 241–276, June 1955.

[31] Mirko Leomanni. *Attitude and Orbit Control Techniques for Spacecraft with Electric Propulsion*. PhD thesis, 02 2015.

[32] D. S. Liechty, A. J. Wise, S. Subramaniam, and K. A. Stephani. Comparison of CFD and DSMC using calibrated transport parameters. In *31st international symposium on rarefied gas dynamics: rgd31*. AIP Publishing, 2019.

[33] Thierry Magin. Simulation of atmospheric entries of meteors in the continuum and rarefied regimes. Lecture series: hypersonic meteoroid entry physics, October 2017.

[34] Avshalom Manela and Livio Gibelli. Free-molecular and near-free-molecular gas flows over backward facing steps. *Journal of Fluid Mechanics*, 889, 04 2020.

[35] M.Vio, F.Peron, and P.Romagnoni. «lo scambio termico per irraggiamento». In: Corsi di Fisica Tecnica, 2000-2001.

[36] I. Nompelis and T.E. Schwartzentruber. Strategies for parallelization of the dsmc method. *51st AIAA Aerospace Sciences Meeting including the New Horizons Forum and Aerospace Exposition 2013*, January 2013.

[37] Pietro Parodi. Analysis and simulation of an intake for air-breathing electric propulsion systems. Master's thesis, 07 2019.

[38] G. Prisco. Optimization of direct simulation monte carlo (dsmc) codes for vector processing,. *Journal of Computational Physics*, 94:454–466, 1991.

[39] AE Puckett and HJ Stewart. The thickness of a shock wave in air. *Quarterly of Applied Mathematics*, 7(4):457–463, 1950.

[40] E. Sartori and Pierluigi Veltri. Avocado: A numerical code to calculate gas pressure distribution. *Vacuum*, 90:80–88, 04 2013.

[41] Vahid Shariati, Mohammad Hassan Ahmadian, and Ehsan Roohi. Direct simulation monte carlo investigation of fluid characteristics and gas transport in porous microchannels. *Scientific Reports*, 9, 11 2019.

[42] Maxim Vladimirovich Shcherbakov, Adriaan Brebels, Nataliya Lvovna Shcherbakova, Anton Pavlovich Tyukov, Timur Alexandrovich Janovsky, Valeriy Anatol'evich Kamaev, et al. A survey of forecast error measures. *World applied sciences journal*, 24(24):171–176, 2013.

[43] Alessandro Turchi. Development of an enhanced spacecraft fragmentation code technical, implementation, management and financial proposal. June 2021.

[44] Timothy Van Daele. *Model-based analysis as a tool for intensification of a biocatalytic process in a microreactor*. PhD thesis, 12 2016.

[45] Charton Virgile, Awad Albert, and Labaune Julien. Optimisation of a hybrid ns-dsmc methodology for continuous-rarefied jet flows. *Acta Astronautica*, 195, March 2022.

[46] Wen-Lan Wang, Quanhua Sun, and Iain Boyd. Towards development of a hybrid dsmc-cfd method for simulating hypersonic interacting flows. *AIAA*, pages 2002–3099, 06 2002.

[47] Jong-Shinn Wu, Y. Lian, G. Cheng, R.P. Koomullil, and K.C. Tseng. Development and verification of a coupled dsmc-ns scheme using unstructured mesh. *Journal of Computational Physics*, 219:579–607, 12 2006.